A Study of Crystallinity in the Blue Dragon Lava Flow and the Ross Flow Using Visible
Near-Infrared Spectroscopy

A Thesis

Presented in Partial Fulfillment of the Requirements for the

Degree of Master of Science

with a

Major in Geology

College of Graduate Studies

University of Idaho

by

Kari Odegaard

Major Professor: Erika Rader, Ph.D.

Committee Members: Leslie Baker, Ph.D.; Thomas Williams, Ph.D.

Department Chair: Jerry Fairley, Ph.D.

August 2021

Authorization to Submit Thesis

This thesis of Kari Odegaard, submitted for the degree of Master of Science with a Major in Geology and titled "A Study of Crystallinity in the Blue Dragon Lava Flow and the Ross Flow Using Visible Near-Infrared Spectroscopy," has been reviewed in final form. Permission, as indicated by the signatures and dates below, is now granted to submit final copies to the College of Graduate Studies for approval.

Major Professor: _____ Date: 7-30-21

Erika Rader, Ph.D.

Committee Members: _____ Date: 7-30-2021

Leslie Baker, Ph.D.

_____ Date: 7-30-2021

Thomas Williams, Ph.D.

Department Chair: _____ Date: 07.30.2021

Jerry Fairley, Ph.D.

Abstract

Lava flows are volcanic hazards that have emplacement pathways and speeds that are difficult to predict. One variable that contributes to this unpredictability is the viscosity of the flow which changes by several orders of magnitude from eruption to solidification. To accurately estimate viscosity we must know the temperature, geochemistry, crystal content and vesicularity of the lava. While temperature and geochemistry can be quickly and safely assessed using a thermal camera and portable x-ray fluorescence spectrometer (XRF), crystal content and vesicularity require sample collection and microscopy. We propose that visible near-infrared spectroscopy (VNIR) can inform viscosity estimates with rapidly collected mineralogic data. Previous studies have used VNIR spectral features to distinguish mafic glass from olivine and plagioclase in basalt in laboratory settings. We test a handheld in-situ instrument protocol to estimate crystallinity on the Blue Dragon lava flow (BD) and the Ross Flow (RF), selected for their differing sizes, crystallinity, and vesicularity to determine the sensitivity of the instruments and any limitations. XRF was used to obtain bulk geochemistry. Samples were collected and the proportion of phases are identified from scanning electron microscope backscatter images. The prominence of VNIR absorbance features positively correlates with increased crystallinity. Both BD and RF show increased reflectance with an increase in crystallinity. The potential for improved modeling of lava flows for hazard management with remote VNIR rests on the instruments ability to detect typical ranges of crystallinity in natural lava. If successful, these spectrometers can be attached to high resolution satellites or drones for safe and distant data collection in real time.

Acknowledgements

Table of Contents:

List of Tables

List of Figures

Part 1: Introduction

1.1 The importance of lava flows

Lava flows contain a wealth of information that can be applied to hazard management, the study of other rocky bodies in our solar system and beyond, and the complex story of the Earth. Lava originates as magma that is then erupted from a vent or fissure and forms a flow. There is a range of lava flows that vary in silica content from mafic basaltic flows to the felsic rhyolitic flows (Winter 2010). The far-reaching lava flows that are found throughout the world in places such as Indonesia, Iceland, and Hawaii are basaltic lava flows. Being mafic in composition the silica content is low and has a lower viscosity which facilitates flow (Winter 2010). Even though lava is one of the least immediately dangerous volcanic hazards, it can be highly destructive to property and surrounding communities. Mafic lava flows are capable of flowing long distances, as can be seen in Hawaii from the Pu'u O'o lava flows, in part due to their low viscosity. Constraining viscosity of mafic lava flows gives insight into the distance they may travel (Turner et al. 2017).

Lava flows hold plenty of information consisting of chemistry of the magma chamber, transport, emplacement and more. Of this information, viscosity is often used to understand how lava flows move by using specific variables. These variables consist of temperature, crystallinity, geochemistry, and vesicles (Harris & Allen III 2008, Stasuik et al. 1993, Diniega et al. 2013, Vetere et al. 2013). Viscosity, a resistance to flow, determines how and how fast a lava flow moves as the variables change between the vent and its emplacement. Knowing viscosity and the variables that control it aids in predicting the movement of active lava flows. This is important for hazard management in planning evacuations and in the case of Iceland currently, where to place lava barriers to protect important roads and predict the likely path of the flowing lava.

1.2 Viscosity

Viscosity is a measure of resistance to flow. A fluid with low viscosity will have a low resistance to flow and a fluid with high viscosity will have the opposite. In lava,

the viscosity is controlled by crystallinity, temperature, vesicles, and geochemistry (Harmon et al. 2000, Harris & Allen III 2008, Stasuik et al. 1993, Diniega et al. 2013, Vetere et al. 2013). In an active lava flow each variable can change and affect viscosity, which creates difficulties in correctly modeling a lava flow. Simple laboratory analogues are used to measure specific parameters to understand how the fluid would behave if a single, or a select few, variables were changed such as temperature or a change in silica content (Harmon et al. 2000, Harris & Allen III 2008).

One of the major controlling factors in viscosity is temperature, a commonly manipulated variable (Harmon et al. 2000, Harris & Allen III 2008). Variances in temperature as a lava is flowing influences the flow speed due to increasing viscosity with decreasing temperature (Stasuik et al. 1993). Changing temperature also affects the crystals within the melt. As the temperature decreases from the vent to emplacement, phenocrysts grow and microlites can form.

With nucleation and growth of crystals, the geochemistry of the surrounding melt is depleted of elements composing the crystallizing microlites and growing phenocrysts (Winter 2010). Beyond the crystal's growth and nucleation, differences in silica content due to differences in the source magma between different lavas influences the viscosity as well. As silica increases, magnesium and iron decrease, which in turn increases viscosity (Griffiths 2000, Chevral et al. 2018, Stasuik et al. 1993). The low silica and high magnesium and iron content melts are mafic with a low viscosity and high temperature. Meanwhile, the higher silica content and lower magnesium and iron content lavas like dacite and rhyolite have higher viscosity and lower temperature. This example shows that geochemistry is not varied in models and experiments on viscosity as it is assumed that the bulk geochemistry will not change through a flow's activity. Yet, at Kilauea in the 2018 eruption the silica content changed due to magma assimilating three different existing sources of melt (Gansecki et al. 2019). Two sources had interacted with residual old pockets of magma from Kilauea's east rift zone. The assimilation of older and more evolved magma led to fissure eruptions of andesitic basalt. The third source erupted from fissure 8 with a

similar basalt composition that was erupted at Kilauea's summit prior to 2018. The third source produced an effusive eruption (Gansecki et al. 2019). The change in silica content of these lavas within the same volcanic system changes the viscosity with the andesitic basalt being more viscous and creating a more explosive eruption. Geochemistry, in terms of silica content, can change between different lava flows, from different vents within the same lava flow and even within the phenocrysts themselves (Gansecki et al. 2019, Stasuik et al. 1993).

Within basalts there is a variance of vesicle density denoting the amount of trapped volatiles that failed to escape (Winter 2010). Vesicles created from the trapped gases increase viscosity (Greeley et al. 2005, Chevral et al. 2018). As degassing occurs within a lava flow, undercooling may occur and facilitate an increase in crystal growth, further increasing viscosity (Pinkerton & Sparks 1978, Sahagian 1985, Shea et al. 2010).

Viscosity, a resistance to flow, is controlled by the geochemistry, temperature, crystals, and vesicles within a lava. As the temperature decreases during flow the viscosity is increased until emplacement. With the growth of phenocrysts and nucleation of microlites the matrix is depleted of the elements required to form the crystals and increases viscosity. The trapping of vesicles within a lava increases the viscosity and undercooling caused by degassing may facilitate further crystal growth to further increase viscosity.

1.3 Visible Near-Infrared Spectroscopy

VNIR or visible near-infrared is a section of wavelengths within the electromagnetic spectrum. The electromagnetic spectrum itself can be broken into sections of wavelengths of energy that span from radio waves, the longest, to gamma waves, the shortest (Butcher 2016). VNIR can be broken down to the wavelengths for visible light and the range of infrared wavelengths called near-infrared. Visible light encompasses a small portion of the electromagnetic spectrum with wavelengths of between 380 nm to 700 nm and is the only light that is detectable by the human eye (Butcher 2016). Near-infrared follows the red visible light and ranges from 700 nm to

1,400 nm wavelengths and the shortwave infrared often included in VNIR spans to 2,500 nm (Butcher 2016, Tiruneh 2014). Both the visible and near-infrared make up VNIR which typically ranges from ~400 nm-2,500 nm (Tiruneh 2014, Butcher 2016).

VNIR spectroscopy functions by measuring the tendency of molecules to absorb electromagnetic radiation in the VNIR spectrum. Light in the range of VNIR is shot at an object or surface and the instrument will record what is reflected and what is absorbed by that object (Tiruneh 2014, Butcher 2016, Pour et al. 2018). Reflectance occurs when incidence light encounters and object and is returned or reflected (Tiruneh 2014, Butcher 2016). Absorbance occurs as energy in the VNIR spectrum interacts with a surface. The molecules of the surface vibrate or electronic transition process raises electrons in molecules to a higher power thus creating a specific pattern in the spectrum (Tiruneh 2014, Butcher 2016, Rowan et al. 2003). These absorbance features in VNIR spectra can serve as a fingerprint to identify materials as each atom and molecule has a corresponding absorbance (Tiruneh 2014). This identification provides a nondestructive process of gathering spectral data, which is important for limited samples or areas where samples are impossible to retrieve (Pour et al. 2018, Tiruneh 2014, Adamalik 2020).

Glass is an amorphous solid and is a component of basaltic lavas and within the glassy matrix phenocrysts, microphenocrysts or microlites are found (Scudder et al. 2021, Winter 2010, Cannon et al. 2017). Studies done on varying chemistries of glass has shown that a change in the Fe content will change the spectra (Carli et al. 2016, Scudder et al. 2021). An increase in glass and glass grain size in these studies show a lowering of the reflectance spectra and in some cases a flattening as well attributed to the amorphous properties of the glass (Carli et al. 2016, Scudder et al. 2021, Serventi et al. 2013, Cannon et al. 2017). Within basalt there are typically phenocrysts of minerals such as pyroxenes, olivine and plagioclase which can serve to impact the spectra through reflection as they are not amorphous like the glassy matrix (Winter 2010, Carli et al. 2016, Reeder 2020, Serventi et al 2013). Minerals within a glassy matrix in basalt create absorbance features within the spectra according to their

geochemistry (Serventi et al. 2013). Minerals such as the pyroxenes have absorbances at ~ 1000 nm and a broader absorbance dipping at ~2250 nm wavelengths (Carli et al. 2016, Carli et al. 2015), whereas changes in olivine show a wider absorbance feature between 1000 nm to 1500 nm wavelength (Serventi et al. 2013). Studying basalt through the VNIR spectra of glass and the minerals that compose the lava provide insight into which absorbance features are important to search for and can be applied to not only laboratory spectra, but also other VNIR that is used.

1.4 Visible Near-Infrared Spectroscopy in Space

Beyond its use on Earth, VNIR has been used for studies of our solar system and beyond as a way to access and understand the lithologies present without requiring sample return missions (Serventi et al. 2013, Carli et al. 2018, Black et al. 2016, Carli 2009, Sanchez 2014). Studies on rocks used with VNIR for a look into space are done using satellites or in labs utilizing analogs or meteorites, such as diogenites (Serventi et al. 2013, Carli et al. 2018, Black et al. 2016, Carli 2009, Sanchez 2014).

A rare, yet important component of understanding the geochemistry of other planets and extraterrestrial bodies is through the pieces that are cast off and land on Earth as meteorites. Work has been done on mafic meteorites such as shergottites, nakhlites, and diogenites with VNIR spectra (Hiroi et al. 2011, Carli et al. 2018, Harris & Grindrod 2018). These meteorites are mafic in composition and VNIR is used to identify the composition (Hiroi et al. 2011, Carli et al. 2018, Harris & Grindrod 2018). Carli et al 2018 studied a diogenite, a Vesta meteorite, and used VNIR spectra to identify absorbance bands associated with the olivine and pyroxene present in the sample. Testing slabs and powders of the diogenite they were able to identify specific absorbance features unique to the present pyroxene and the abundance of olivine. Thus, specific mineral compositions are detectable in VNIR (Carli et al. 2018).

Meteorites offer a wealth of information, but they are a highly limited resource, while Earth analogs are accessible and can be relatively easily studied. Analogs can be naturally generated materials, like Icelandic basalt flows (Ehlman et al. 2012, Carli 2009), or be lab generated materials (Cannon et al. 2017, De Angelis et al. 2014). The

benefits to working with an analog is not only the accessibility but also the controlled environment. Using what is available to study extraterrestrial bodies on Earth and compare the spectra of the analog experiments with those of the targeted bodies allows a look into their geology. This project studies two lava flows on earth with different sizes, minerals, and complexities to test VNIR in-situ.

1.5 Goal of project

The overarching goal of the project is to use visible near-infrared spectroscopy (VNIR) in-situ on lava flows and determine if reflectance increases with increased crystallinity on two separate lava flows. If reflectance increases with increased crystallinity, then this technique can be applied to future endeavors on active lava flows and on extraterrestrial bodies. I evaluate the crystallinity percentages within two lava flows through image analysis and compare them with VNIR reflectance that was gathered in the field. The two lava flows that were chosen were the Blue Dragon lava flow from Craters of the Moon National Monument & Preserve and the Ross Flow of Lava Beds National Monument. Spectral analysis using an ASD Terraspec Halo VNIR was performed on both flows. In theory as lava distances itself from the vent, viscosity will increase from decreasing temperature and increased crystallinity through crystal growth and microlite nucleation (McClinton et al. 2014, Cashman et al. 1999, Vetere et al. 2013). An assumed cooling history can be attributed to lava flows with this theory in mind where a margin of a lava flow experiences the smallest change in temperature and the vent experiences the largest change in temperature

With the increasing crystallinity there will be less glass that is amorphous and refracts light. As crystallinity increases it is expected that reflectance from the VNIR will increase as well as less light will be refracted from the glass. If this holds true, then VNIR could be used to infer changes in crystallinity in the field with similar remote sensing tools or on drones and satellites for inaccessible or less accessible lava flows.

1.6 Blue Dragon

The Blue Dragon lava flow is one of the many lava flows that populate Craters of the Moon National Monument and Preserve (COTM) in the eastern Snake River Plane of Idaho (figure 1). COTM sits over the Great Rift and the volcanism in the area had fed cinder cones, spatter cones, and various lava flows (Chadwick et al. 2019, Kuntz et al. 1982). It was named thus due to the tinge of blue and purple that color the surface of parts of the lava flow (Faye & Miller 1973, Chadwick et al 2019). The Blue Dragon lava flow (BD) is one of the youngest lava flows at COTM with an age of 2076 ± 45 years B.P. (Chadwick et al. 2019, Kuntz et al. 1986, Putirka et al. 2009). The lava flow is expansive and spans an area of 280 km^2 southwest of
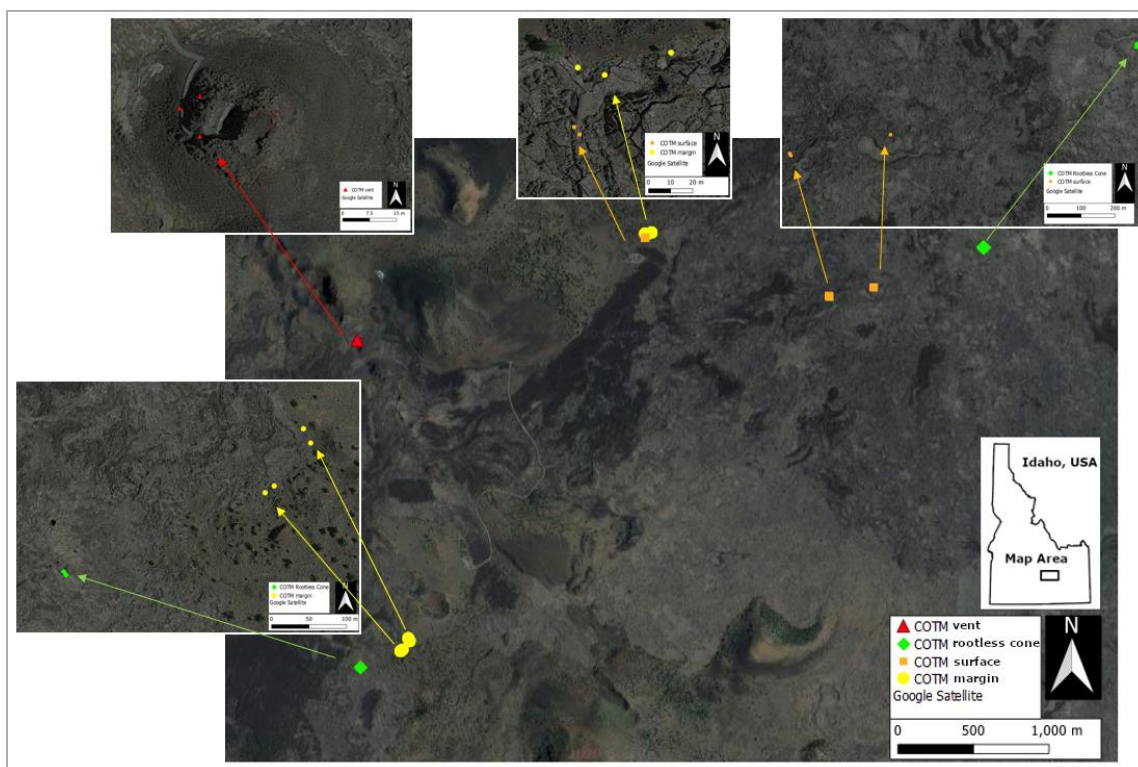
Figure 1: Map of sample locations for the Blue Dragon Lava flow

Big Cinder Butte (Chadwick et al. 2019). The BD pahoehoe basalt flow is an extensive flow that has numerous lava tubes that fed its current emplacement (Chadwick et al. 2019, Kuntz et al. 1982). Within BD there are places where a lava tube had sprouted a feature called a rootless cone, an eruptive area that is not directly fed

by the magma source (Kuntz et al. 1982, Rader et al. 2018). Surface texture and roughness varies along the surface of BD (Chadwick et al. 2018).

BD was determined to be a trachybasalt, an intermediate between trachyte and basalt containing both plagioclase and alkali feldspar, from geochemical analysis with microphenocrysts of olivine, plagioclase, titanium magnetite and apatite (Chadwick et al. 2019, Leeman et al. 1976, Kuntz et al. 1985, Faye and Miller 1973). According to Chadwick et al. 2019, BD can be broken into five phases differentiated spectrally, geochemically, and through field observations by variances in surface color. There is

Figure 2: Smooth pahoehoe surface with green ring for scale.

a range in SiO_2 wt % for BD of 51.8 wt % in phase 1 to 48.5 wt % in phase 5 (Chadwick et al. 2019). The surface of BD varies in colors from dark grey black to a range of purple and blue to light blue from the reflection of titanian magnetite at the surface (Faye and Miller 1973). Figure 2 shows an area of pahoehoe from BD with the dark blue to purple color associated with the lava flow.

On large and/or long basalt flows like BD the erupting lava forms a thin crust that has flowing lava beneath it to create a lava tube for transport. Recently lava tubes have been observed in the Pu'u O'o lava flow in Hawaii (Heliker et al. 2003, Chadwick et al. 2018). For BD, these lava tubes also gave way to rootless cones or hornitos caused by unsteady flow and a breaking of the tube's roof (Heliker et al. 2003). Lava tubes are often formed in one of two ways, 1) from the solidifications of a crust over a channel and 2) a concentrated flow inside an inflating lobe (Keszthelyi 1995). As the lava is travelling through these tubes, it is insulated from the outside air and other elements. In the case of some Hawaiian flows, the cooling rate of the lava tubes is 1° C per km which allows for long distance transport (Keszthelyi 1995). The slow cooling from lava tubes also slows the increase in viscosity. This can then play a role in the growth of crystals within the lava and perhaps stalled their growth (Winter 2010).

1.7 The Ross Flow

Situated in Lava Beds National Monument the Ross Flow (RF), also called the Ross Chimneys (fig 3, 4), is a small lava flow about 1 km long and is part of the Medicine Lake volcanic center in Northern California. 3080 years B.P. porphyritic basalt erupted at the Ross Flow from a fissure eruption just north of Black Crater to create small
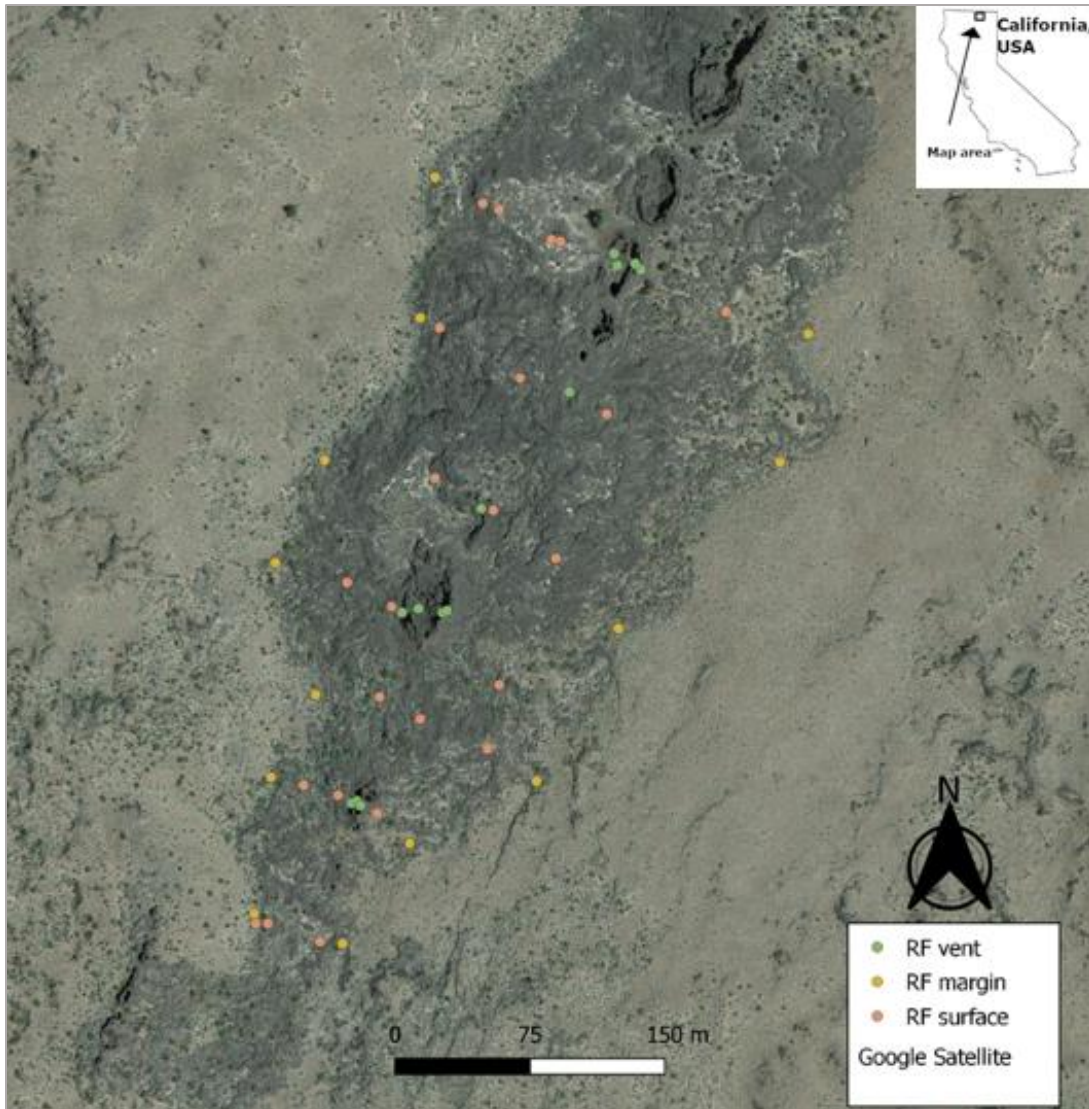
Figure 3: Map of the Ross Flow with denoted sample spots

pahoehoe flows and spatter vents (Donnelly-Nolan et al. 2007, Nathenson et al. 2007, Donnelly-Nolan 2010). RF was a short fissure eruption that resulted in ~1 km long flow and formed numerous spatter vents (Donnelly-Nolan et al. 1990). The basaltic composition of this flow is 48.3 to 49.6% SiO_2 (J. M. Donnelly-Nolan 2010). Abundant phenocrysts of plagioclase with olivine exist in a glassy vesiculated matrix. On the surface of the lava flow there is white to off-white air fall pumice from either Glass Mountain or Little Glass Mountain (Donelly-Nolan et al. 1990).

Figure 4:The vent at the Ross Flow that has also been called chimneys.

1.8 Cooling History

Both BD and RF can be broken down into areas according to assumed temperature gradient: margin, vent, surface, and rootless cone (hornito). Of these classifications RF does not contain any rootless cone features. A margin is assumed to be the edge of the flow and experienced the lowest temperature as it is the furthest edge of the emplaced lava flow where viscosity increased enough to halt movement. The surface is assumed to be an intermediate temperature between margin and vent where viscosity was increased until it reached the margin. Vents are where lava erupted and are assumed to have experienced the highest temperature with the lowest viscosity before emplacement. Rootless cones are assumed to have an intermediate temperature between surface and vent as these features are composed of erupted lava from a broken lava tube and possible interaction with water (Rader et al. 2018, Fagents & Thordarson 2007, Bruno et al. 2004). In addition, the vent would cool

quickly enough to halt growth of crystals within the melt, while the margin had a longer time to cool facilitating growth of crystals (Winter 2010). The surface and rootless cone are assumed to be intermediary between vent and margin. Yet, these categories do not take into consideration the complexity of a lava flow like BD which has extensive lava tubes which provided insulation to the lava when it was actively flowing (Dineiga et al, 2013, Chadwick et al. 2019).

Currently there is a basaltic eruption in Iceland which had formed a complex lava flow fed by multiple vents and fissures with lava transport facilitated by lava tubes and channels (Reykjanes Peninsula 2021, Global Volcanism Program 2013). While observing this volcanic eruption via multiple live feeds from YouTube, the surface is often overrode with new lava and margins may not represent the last to cool. These assumptions are biased to simple flows like RF which do not take into account insulation of lava tubes and layering of longer-lived lava flows.

1.9 Purpose

Using reflectance spectroscopy, such as VNIR, is not a new practice, but I am intending to use it in a new way that provides a steppingstone for future work within hazards or even on other planets. Utilizing VNIR on BD and RF will provide insight to how sensitive the portable instrument used is on lava flows of differing sizes, petrology, and color. The aim is to determine if reflectance increases with an increase in crystallinity and to determine if crystallinity increases from vent to margin. RF is a small, yet simple flow with spatter cones at its center and no lava tubes like is seen at BD. Meanwhile, BD is a large lava flow with distinguishable phases, lava tubes, and rootless cones. The mineralogy within BD is different from RF in that it has the presence of oxides and apatite in addition to the plagioclase and olivine. Not all basaltic lava flows are the same, as seen with BD and RF, and utilizing VNIR on them will further demonstrate what is expected to be found spectrally with similar flows on Earth or beyond.

Part 2: Methods

2.1 Field Methods

We chose the BD and RF field sites in order to use VNIR on two different basaltic lava flows to test if the measured reflectance increases with crystallinity. Samples were chosen by locating glassy surfaces with no visible lichen or weathering. Once a spot was located details such as surface roughness, petrology, location, measurement numbers and sample condition were recorded in a field notebook and then subsequently made into a digital copy (see appendix tables 1 & 2). Sample spots were broken into one of four categories related to the hypothesized cooling of the lava flow: margin, surface, rootless cone (hornito), and vent.

Only the smoothest, glassiest surfaces were chosen for optimal use of the instruments to prevent scattering due to a rough surface. Broken and interior areas were not sampled beyond what was collected in hand samples. Hand samples were taken from BD when the sample was able to be extracted without damage to the measured surface. At RF, samples were collected by Dr. Erika Rader with assistance of a park ranger after the original field season. Samples were located by field photo when recognizable. For each sample stop a GPS position was taken and recorded into the field notebook.

Each sample is labelled in the notebook and database according to the flow, year, sample, and spot number with the exception of RF. For example, a Blue Dragon sample is labelled as BD19-04-S3. The Ross Flow sampling was systematic as traverses were made across the lava flow 50 m apart, denoted by GPS, until the day was cut short for lack of water and drained instrument batteries. Each traverse had two measurement spots taken at the margin and at least three between the two margins (fig 4). The naming of samples for the Ross Flow replaced the sample number with a traverse number and removed the S for spot, denoted by T#-#. The reasoning behind using the traverse method on the Ross Flow was due to the flow's small size and the feasibility of using the traverse method that would not function in our favor on the other lava flows due to time and manpower constraints. At each stop three spots, one

sample in BD had four spots, were designated for the sample and circled using colored plastic rings. These plastic rings were used to denote the sample spot so that each instrument would measure the same area. We used GPS, VNIR, and x-ray fluorescence (XRF) at each chosen sample spot. Triplicate analysis was taken with each instrument at each individual spot.

2.2 Visible Near-Infrared Instrumentation

The specifications of the ASD TerraSpec Halo are listed in table 1 and taken from Sehlke et al. 2019 with their study of the instruments and how they function in a field setting with varying surface roughness.

Table 1: VNIR specifications used on the ASD Halo

Spectral range (nm)	350-2500
Spectral resolution	3 nm @ 700 nm 9.8 nm @ 1400 nm 8.1 nm @ 2100 nm
Height x width x depth	31 x 10 x 30 cm

When taking measurements, the sample spots of ~18mm in diameter are illuminated with an internal quartz tungsten halogen bulb (Sehlke et al. 2019). The instrument measures 100 spectra in ~15 s depending on the setting on a bright or dark surface and displays the average continuous spectrum upon its completion (Sehlke et al. 2019). The spectrometer has an internal mineral library that provides a qualitative assessment of identified minerals with an algorithm to indicate the interpretation confidence.

2.3 VNIR in the Field

To measure reflectance in the VNIR, we used a portable ASD TerraSpec Halo. It was transported in the field via a hip holster. Calibration of the instrument was completed before each day of field work using a white spectralon reference that attached to the

face of the instrument. An internal reference was checked every 5-10 analyses. VNIR measurements were taken in a shadow to limit the bias of sunlight in the spectra via measuring in shadows or blocking the sunlight with a hand or body. Any movements or insufficient shielding was recorded in the field notebook and extra measurements were taken when this occurred to retain continuity. Products from the portable spectrometer were saved and then transposed into an Excel file for ease of use and organization. The data was broken up by lava flow into separate files.

2.4 X-Ray Fluorescence Instrumentation

The second instrument used for in-situ measurements on BD and RF was a portable X-ray fluorescence spectrometer (XRF). The XRF used was a Bruker Tracer IV-SD® and works by emitting a beam to penetrate the target sample and emits a secondary X-ray that is measured to acquire the elemental composition of a sample. Collected data is stored in the instrument until it is extracted and later interpreted to correspond to a geochemical composition. In conjunction with the specifications listed in table 2, a ~10 mm-thick prolene window protected the X-ray tube and detector from contamination. An internal filter wheel can be used for optimization for specialized measurement conditions, but filters were not used in 2019 with the IceCrystal team. (Sehlke et al. 2019)

Table 2: XRF specifications (Sehlke 2019)

Anode current	60 mA @ 40 kV
X-ray beam	Rh target thin window
Secondary electron count	10 mm^2 X-Flash silicon drift detector

2.5 XRF in the Field

This instrument measures the bulk geochemistry of the targeted spot. XRF was used to identify geochemistry and to support the data of the VNIR. The same spots for each sample were targeted using the XRF, which was operated by Dr. Alex Sehlke, as he was the sole possessor of the license to operate the instrument. Like the operations with the VNIR, triplicate analyses were taken using the XRF on the

designated spot. Measurement ID numbers were recorded in the field notebook for data retrieval and organization.

2.6 Field Limitations

While working in the field, limitations with the instruments and sample collection occurred. The limitations for the VNIR and XRF consisted or battery usage, portability, and limited replacement parts. The VNIR was a large instrument carried in a hip holster with additional battery packs. While the VNIR is portable, the weight and bulk of the instrument had an impact on mobility and stamina of the user.

There were technical difficulties using the XRF that had been encountered in the field. The prolene window was somewhat delicate and had to be replaced a few times during the 2019 field campaign due to it cracking and being scratched by the samples it came into contact with. Battery life played a factor as well as on long field days the batteries would need to be replaced in the field. Saved data on the instrument caused a problem with BD as none of the data that had been taken in the field was saved properly and we were unable to retrieve it.

2.7 Lab Methods

After the data was collected in the 2019 field season, data analysis and lab work began. To start this process all hand samples had to be labelled and cut into billets for them to be made into thin sections. The billets were sent to be professionally made into thin sections, many of which returned to be thicker than 30 microns. The samples were then imaged by a scanning electron microscope (SEM) for a close view of phenocrysts and the glassy matrix that surrounded them. For each image, the backscatter emitter was inserted into the SEM to create a back-scatter image. Using backscatter imaging made identifying phases easier due to the difference in greyscale corresponding to the elemental make up of each phase. How backscatter works is by measuring the electrons that were scattered after re-entering the vacuum of the SEM to create a signal (Egerton 2016). Table 3 lists the SEM specifications that were used for each image.

Table 3: SEM specifications

Voltage	20 kV
Working distance	13.0 mm
Magnification	100x, or 300-400x for dendritic samples

A minimum of ten images were taken for each sample with eight being of the rim and two were taken of the interior. Phenocrysts were identified through shape, spot checks, and point IDs. Spot checks are a tool used in the program for the SEM to focus on a single spot and analyze it quickly without scanning an entire image. Point IDs are where an image is taken and only selected spots within the image were analyzed at once. Phenocrysts were identified by shape and spot checks to identify the chemical composition. Point IDs were also taken in which an image was acquired, and multiple points could be chosen and analyzed in the same way that the spot IDs were taken. Point IDs are a function of the SEM which allows the operator to choose a single or multiple point in the sample and use the energy-dispersive X-ray (EDS) to identify the elemental composition below the designated point.

In addition to the point IDs and the spot checks, a single elemental map was completed for each thin section. The images used for the elemental maps are meant to be representative of the different phases in the thin section and taken at 100-400x magnification depending on the size of the phenocrysts and microlites. When making the elemental map, the system scans the thin section multiple times and identifies individual elements and highlights them in a specific color. The more populated a certain color within each measured element is the concentration of the element. An elemental map for a BD sample is shown in figure 5. The elements used to identify each phase were Mg, Fe, Al, Na, P, Ca, and Ti. Olivine was distinguished with Mg and Fe, plagioclase was identified using Al and Na. Overlap of Fe and Ti distinguished oxides and P and Ca was used to identify apatite. Only a singe elemental map was made for each thin section due to constraints on time as elemental maps take ~2

hours to complete. Point IDs and spot checks were used to supplement distinguishing phases as back scatter images were taken.
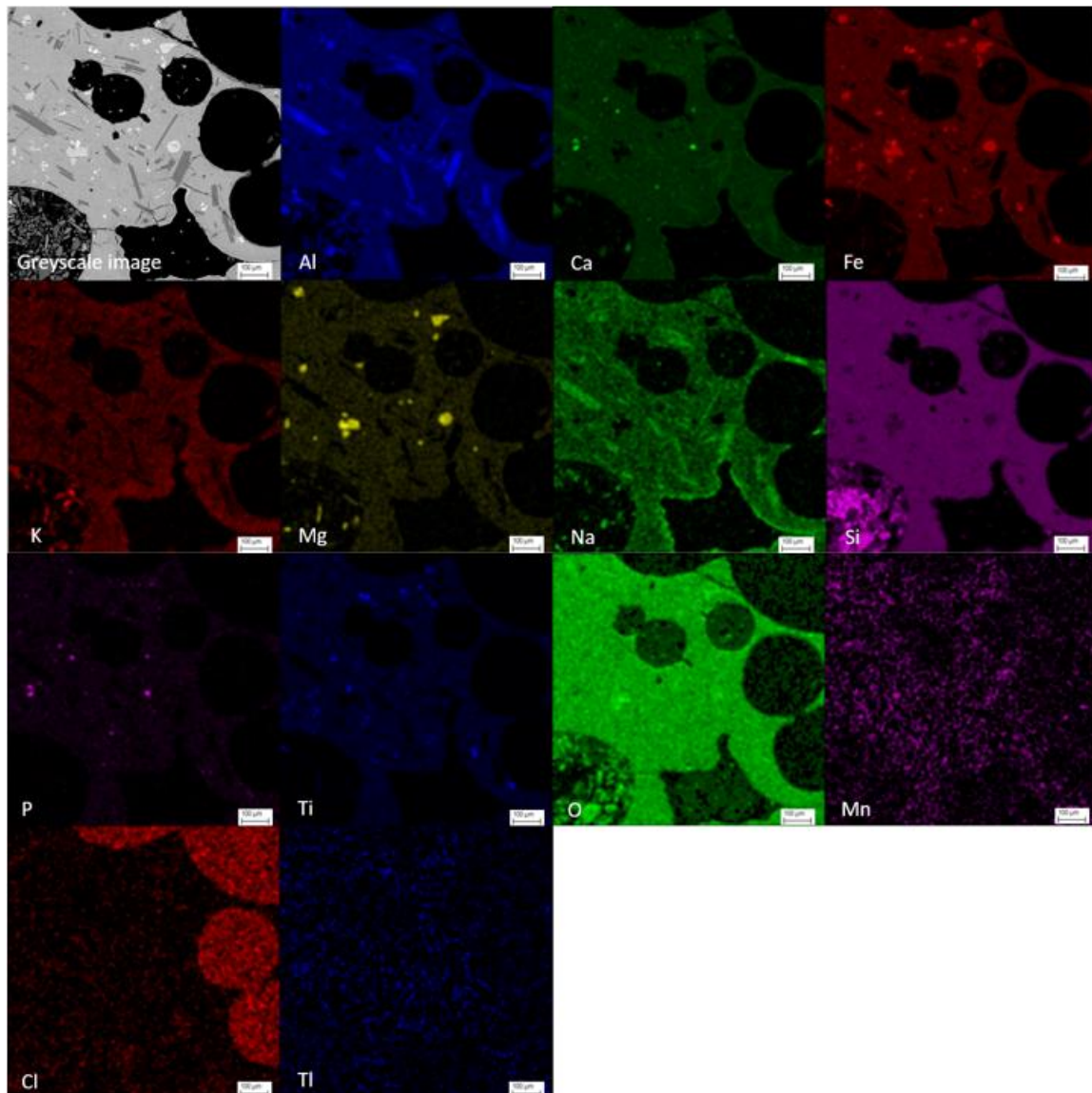
Figure 5: Elemental map of sample BD19-12-S2 taken at x200 magnification.

To acquire a crystallinity percentage, the backscatter rim images were taken into editing programs of either GIMP or ImageJ. A fifty-micron strip along the rim of the sample, measured from the scale bar in each image, was outlined and separated into a new layer. In GIMP this new layer was then coded by color for each mode that was

seen in the thin section. Table 4 shows the colors associated with phenocrysts, glass, and vesicles. The altered and glass was identified using point IDs and a difference in greyscale in backscatter images. The altered phase, found only in BD samples, has a similar elemental make up to the glass, but with a higher silica content. In ImageJ, the threshold tool was used to isolate pixels associated with each phase and pixel totals were recorded. For microphenocrysts of apatite and vesicles in ImageJ, they were outlined and colored white or another color due to the similar greyscale values as other phases.

Table 4: Image processing colors associated with each phase identified

Phase/ mode	Image Processing
Glass	white
Altered	yellow
Vesicles	black
Plagioclase	blue
Olivine	green
Oxides	red
Apatite	Purple/magenta

After the image processing was completed, such as in figure 6 and 7, a table was made in excel for the thin section (see Appendix table 3) and pixels for each phase were counted and recorded. From the pixel counts, a percentage of each mode in the thin section was calculated.
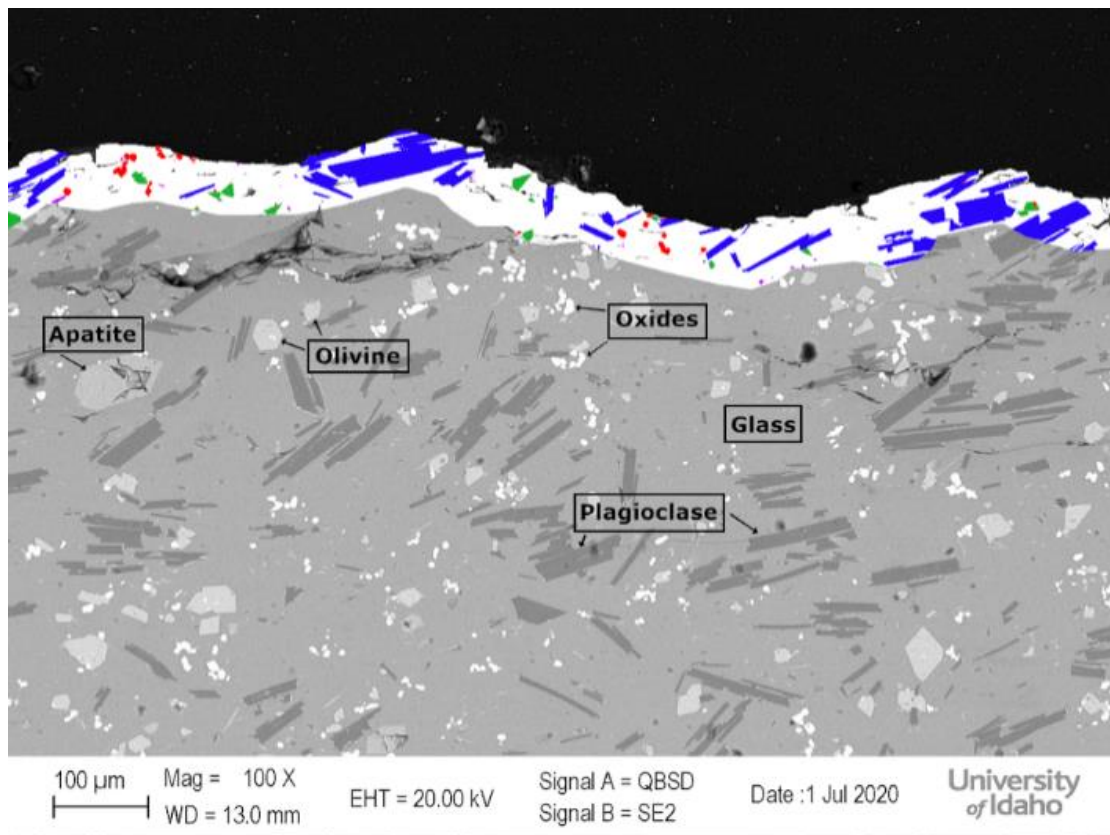
Figure 6: Sample BD19-20-S3 backscatter image with image processing using GIMP to color modes of glass, apatite, plagioclase, olivine, and oxides. Refer to table 4 for color codes.
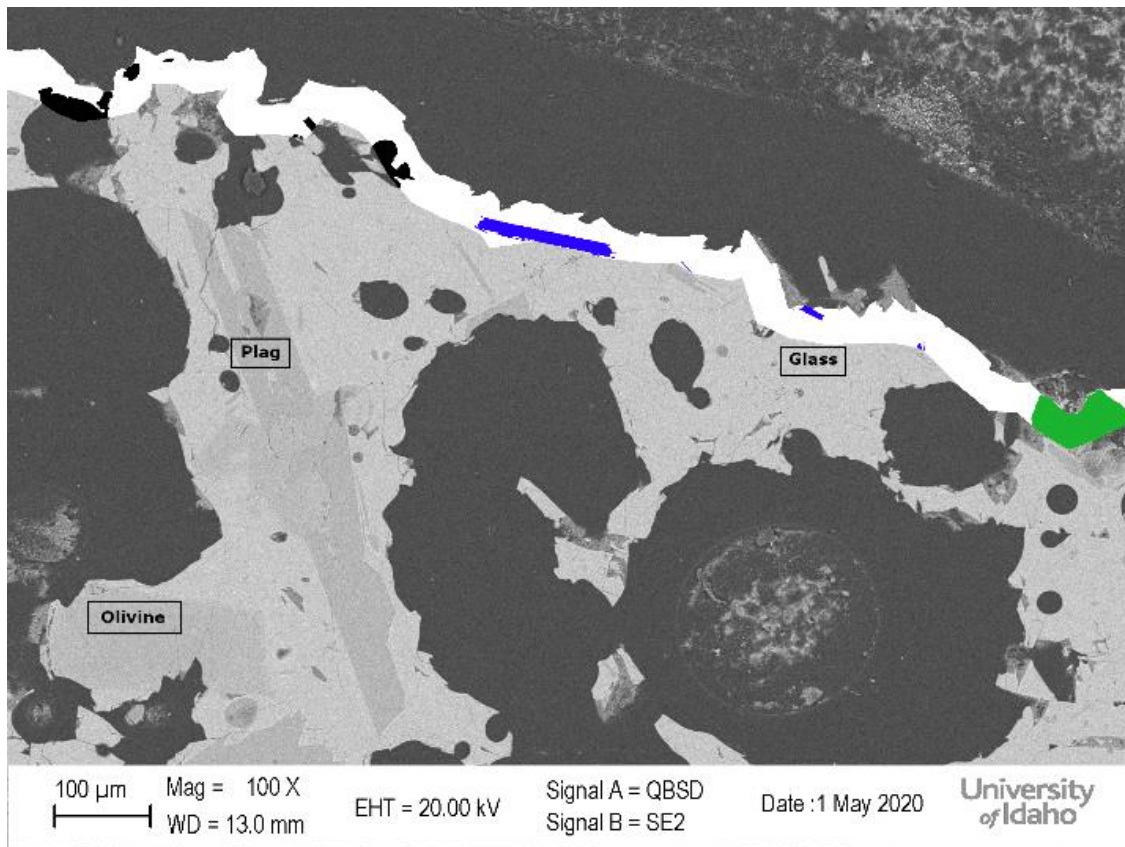
Figure 7: RF19-T2-5 backscatter image with image processing using GIMP to color the modes of glass, plagioclase, and olivine.

After compiling the percentages from the image analysis, a crystal percentage was gained for each sample by making the glass and crystals equal to 100% and discounting the vesicle percentage (table 5). The percentages were then plotted against the average reflectance of each sample using equation 1.

$$Average\ Reflectance = (sum\ of\ reflectance\ 500nm\ to\ 2500nm)/2000$$

Table 5: Average reflectance and crystallinity percents for RF and BD

By location:	Location/ category	Average reflectance	Crystallinity %	Glass %
BD19-19-S1	margin	0.059	24.749	75.251
BD19-20-S3	margin	0.056	18.454	81.546
RF19-T2-8	margin	0.053	16.627	83.373
BD19-15-S3	Surface	0.095	18.118	81.882
BD19-11-S2	surface	0.070	22.050	77.950
BD19-10-S2	Surface	0.075	13.389	86.611
RF19-T4-8	Surface	0.057	20.896	79.104

RF19-T4-2	Surface	0.070	19.080	80.920
BD19-07-S1	vent	0.069	74.113	25.887
RF19-T2-4	vent	0.0648	18.779	81.221
RF19-T2-5	vent	0.0346	12.241	87.759
BD19-12-S2	rootless cone	0.0405	9.411	90.589

Part 3: Results

3.1 Samples Hand and In-situ

We analyzed 61 in-situ spots on BD and collected 15 hand samples from the field. The in-situ measurements in table 6 are each an individual spot measured with VNIR and XRF. Hand samples collected correspond to a numbered spot as it is assumed that the 3 (4 in the case of one margin sample) spots are both close in proximity and composition to warrant only one spot collection. At RF we analyzed 50 in-situ samples and collected 8 hand samples, see table 7. On the RF eight samples were collected after returning to RF with a park ranger for sample collection. A total of 50 samples were analyzed in-situ and spans about 450 m starting from the south side.

Table 6: Blue Dragon collected and in-situ samples

Labels/ categories	In-situ measurements	Collected hand samples
Margin	22	4
Surface	15	6
Rootless Cone	12	3
Vent	12	2

Table 7: Ross Flow collected and in-situ samples

Labels/ Categories	In-situ measurements	Collected hand samples
Margin	14	2*
Surface	23	3
Vent	13	3

The asterisk on the RF margin sample is due to a user error in the field. The hand sample was collected, but any data pertaining to the sample is not included in this study except for a backscatter image to show a texture found at RF.

3.1.1 Blue Dragon Color and Vesicles

The colors of the BD hand samples range from a dark grey-black and blue-violet to a sky blue on the sample surface as seen in figure 8. Black and red colored lava is found at the vents and rootless cones. Blues, blacks, and browns are found at the margin and surface of the BD lava flow. Surface roughness varies between

samples with some samples containing a surface of stretched vesicles, while others are smooth with no vesicles present at the surface (figure 8). The range for surface roughness is <1 mm to 5 mm across the areas sampled.

Figure 8: Field photos of various BD surfaces showing differences in surface roughness and color across the lava flow.

3.1.2 Blue Dragon Petrology

The BD samples are dense with microphenocrysts of plagioclase, olivine, apatite and glomerocrysts/ microphenocrysts of oxides. In certain BD samples (BD19-20-S3 for example) there was an area of alteration at the surface with a higher value of silica than the surrounding glass but was only visible in SEM backscatter images. In the two vent samples phenocrysts are neither euhedral or subhedral but exhibit dendritic textures in the plagioclase and oxides (figure 9). The dendritic plagioclase appears to originate from a single grain that remained within the growth phase longer than the other samples prior to cooling entirely. The dendritic oxides populate these samples between the other microphenocrysts and branch out in feathery dendritic patterns.
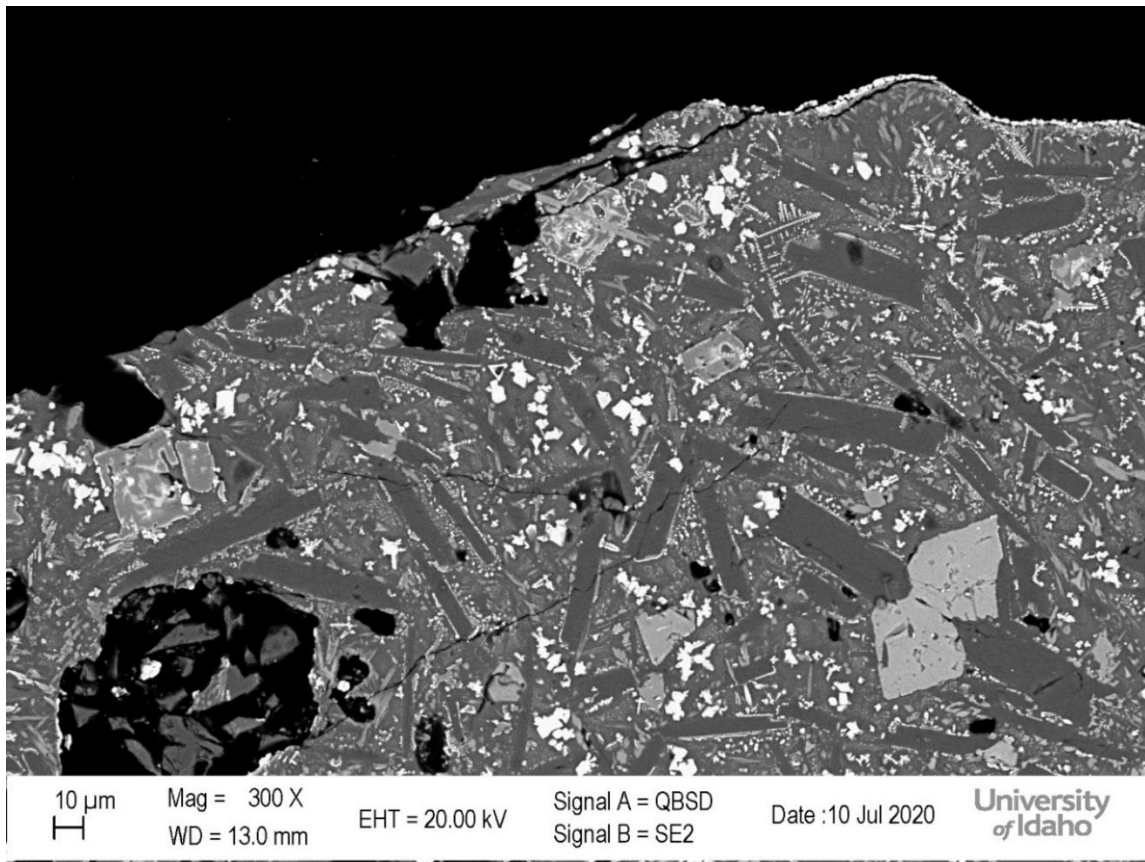
Figure 9: SEM backscatter image of BD19-07-S1 exhibiting the dendritic texture of the oxides

3.1.3 *Ross Flow Colors* and Vesicles

The hand samples are black to dark brown in color at the surface. The color of the surface of samples is found throughout the flow at margin, surface, and vent areas. RF exhibits higher vesicularity than BD and a higher surface roughness. Vesicles are spherical to slightly elongated when not amalgamated into a subhedral coalesced vesicle beneath the rim. The surface roughness varies due to the surface being pocketed by vesicles.

Figure 10: Variances in surface roughness and color found across RF.

3.1.4 Ross Flow Petrology

RF shows large and small phenocrysts of subhedral to euhedral plagioclase and olivine within a glassy matrix. It is common to see glomerocrysts of plagioclase or plagioclase and olivine in RF. There are no signs of oxides within RF or altered glass. Oxide like areas were found in RF but were determined to be products of the thin section process and likely originated from a grinding wheel. Like BD, RF has samples that show dendritic textures within the plagioclase and spinifex-like textures within the olivine. The plagioclase dendritic texture appears to have formed from a single phenocryst and envelops the spinifex-like olivine grains to completely populate the matrix. The dendrites are clinopyroxene with microlites of oxides. The glass is found interstitially between the dendrite branches and phenocrysts.
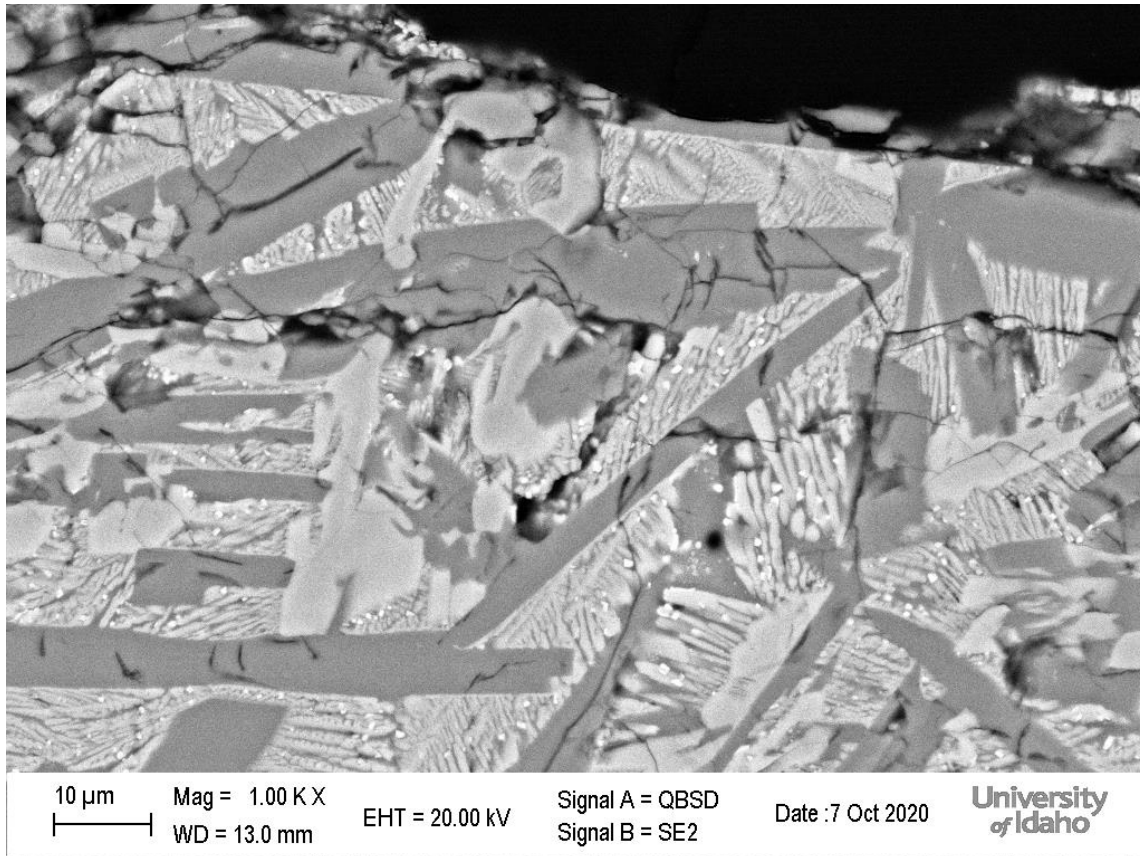
Figure 11: Dendritic texture found at RF along the margin with skeletal olivine, dendritic augite, and oxide microlites. Sample is RF19-T4-9.

3.2 VNIR

The compiled VNIR data was separated into different graphs according to the surface, margin, vent, rootless cone system that was used in the field. The spectra were averaged together for each morphological category. For RF, there was another separation and that was into two weathered sets due to the drastic differences in spectra and were designated into weathered 1 and weathered 2. The difference was determined by shape of the spectra and elevated reflectance. The shape of the spectra in weathered 1 is visibly different from the rest with more distinct absorbance features and a higher reflectance than other spectra by. Basalt typically has flat spectra with a reflectance below 0.1, which sets weathered 1 and weathered 2 apart from the margin, surface, and vent spectra of RF (Hunt et al. 1974, Carli 2009). Weathered 2 Weathered 1 contains 8 samples and weathered 2 contains 7 samples

of the 50 in-situ samples collected. No hand samples were from weathered 1 or weathered 2. The two weathered spectra are shown in figure 12 as the two highest reflectance spectra. The two weathered spectra were not restrained to single category and were found in vent, margin, and surface samples. After the VNIR spectra was separated, only the 500-2500 nm range was used as the 250-499 nm wavelength was unreliable due to instrument constraints. Figures 12, 13, and 14 show the VNIR grouped and graphed with the averaged spectra and an error of 1 sigma contained in the color shaded areas.
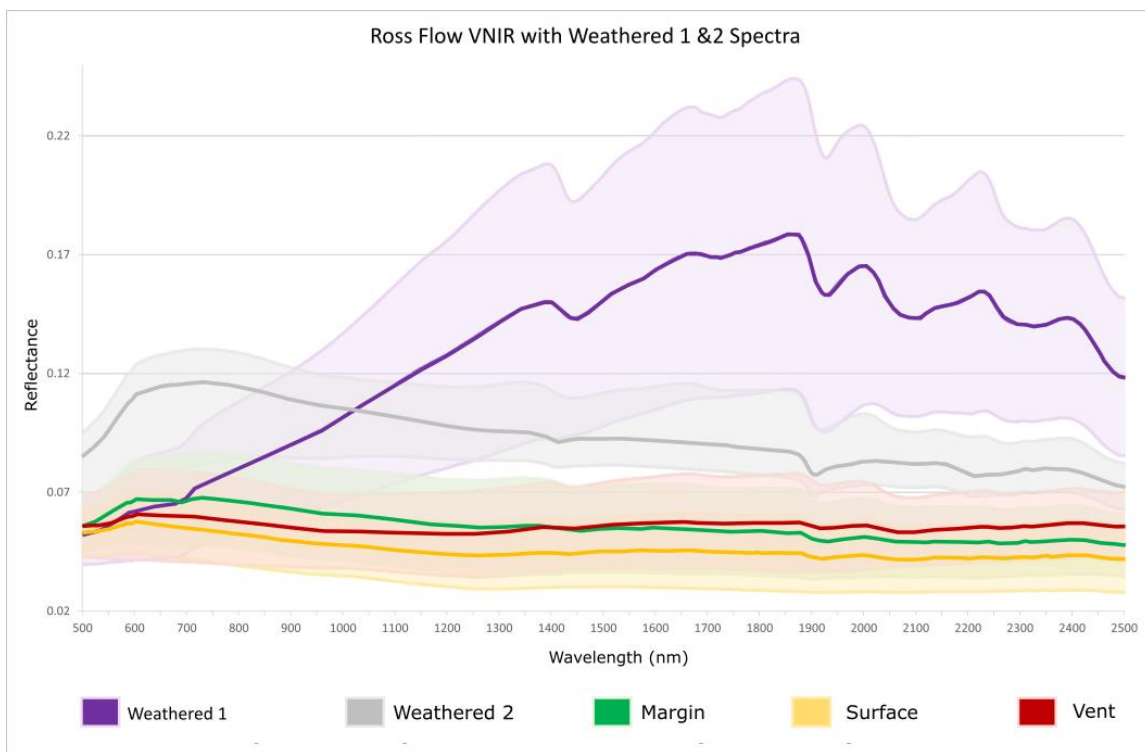
Figure 12: Ross Flow VNIR spectra with shaded areas at a standard deviation of ± 1 sigma.

Absorbance bands were identified as the dips in reflectance across the spectra. Using an online spectral library, absorbances were attributed to water, olivine, or plagioclase (Kokaly et al. 2017). The averaged reflectance of RF ranges between 0.05 and 0.18 as seen in figure 12. In figure 13 absorbances at wavelengths 680 and 2330 are olivine. Plagioclase is associated with absorbances at wavelengths 680, 1005, 1255, 1435, and 2205. Augite absorbance is found at wavelength 1255.
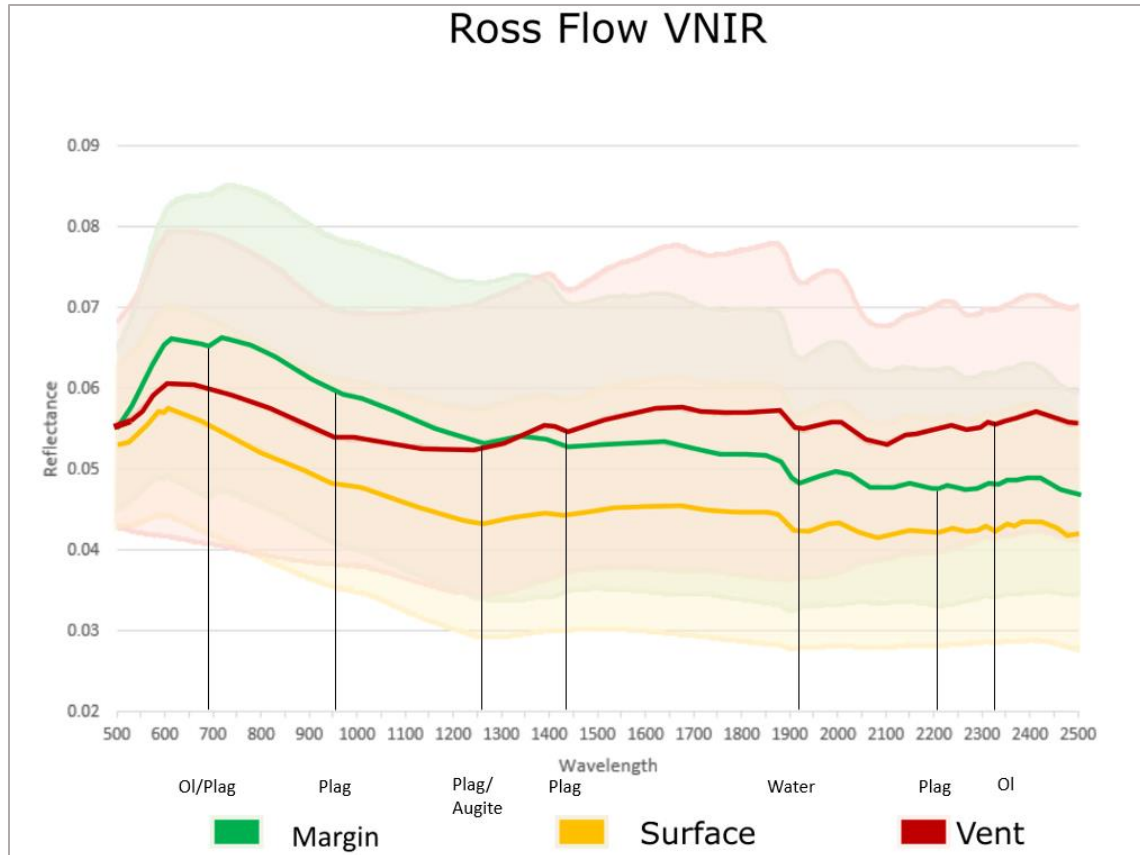
Figure 13: RF VNIR spectra without the two weathered samples and identified absorbance features. Absorbances are associated with minerals and water identified via a spectral library.

Figure 14 shows the averaged VNIR spectra for BD for margin, surface, rootless cone, and vent. Color shaded areas are a 1 sigma error calculated from the reflectance standard deviation. The absorbance features are contributed to found minerals within BD that were identified in the SEM. Plagioclase is associated with absorbances at wavelengths of 680, 950, 1255, 1425, and 2205. Absorbances of olivine are at wavelengths 680 and 2325. Apatite is associated with wavelengths 550, 1425, and 2325. Oxides are present at wavelength 890 and augite at wavelengths 1245 and 2325.
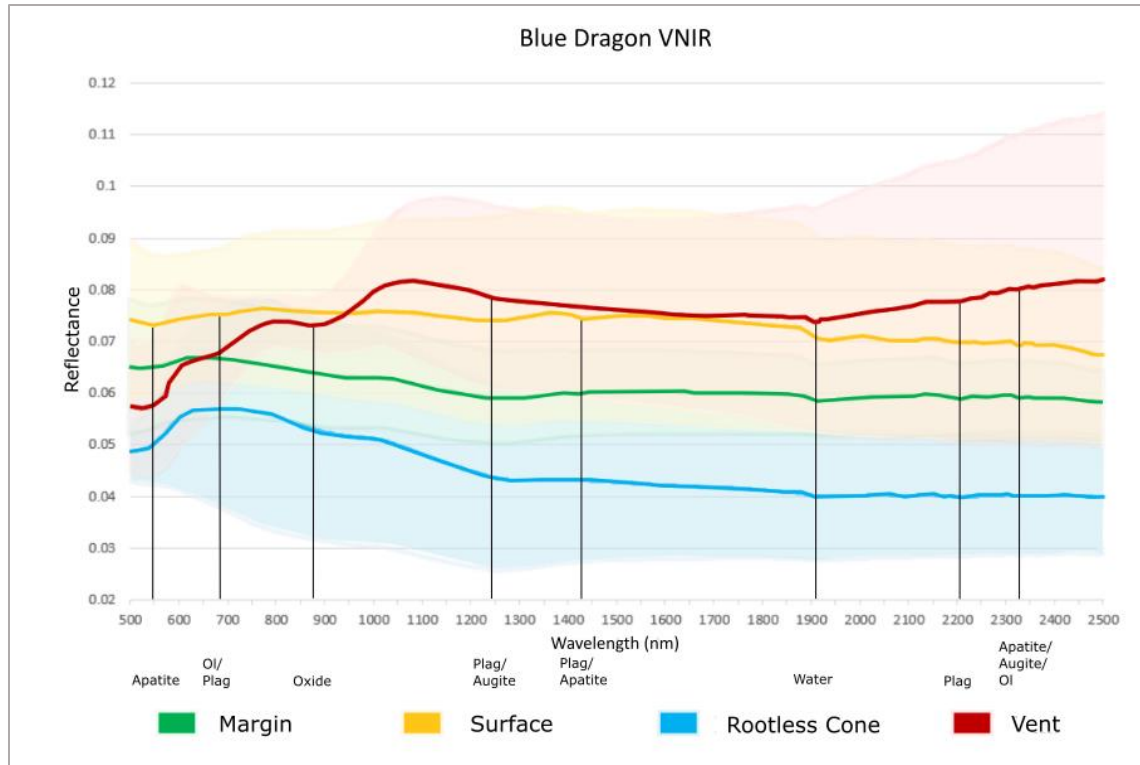
Figure 14: BD average VNIR spectra graph with absorbances identified and labeled from a spectral library.

3.3 X-Ray Fluorescence

The data taken from the XRF was compiled by Dr. Sheridan Ackiss into an excel file. The data used for RF was compiled such that values falling outside of 95%-105% total weight percent were excluded from the data set. Only samples in table 8 were deemed usable and are included.

Table 8: XRF values for Ross Flow

Sample #	Na_2O	MgO	Al_2O_3	SiO_2	P_2O_5	K_2O	CaO	TiO_2	MnO_2	FeO	Total
RF19-T1-1	2.55	7.19	16.90	51.56	0.36	1.45	7.37	0.94	0.26	10.69	99.26
RF19-T1-4	3.07	4.97	13.31	53.37	0.41	1.09	8.70	0.82	0.22	12.27	98.23
RF19-T1-5	3.03	4.54	13.53	52.23	0.46	0.61	9.82	1.10	0.22	11.91	97.45
RF19-T2-3	3.81	5.98	7.59	56.61	0.43	1.34	8.30	0.49	0.22	11.63	96.39
Rf19-T2-4	3.09	5.11	11.36	53.72	0.31	0.73	10.30	1.10	0.20	9.79	95.72

RF19 -T2-5	2.79	4.93	15.09	51.34	0.23	0.58	10.87	1.33	0.20	10.35	97.70
RF19 -T2-6	2.31	7.70	14.06	49.44	0.57	0.41	10.90	1.20	0.21	11.00	97.80
RF19 -T2-7	2.72	9.24	14.32	48.44	1.36	1.54	9.05	0.90	0.20	9.64	97.42
RF19 -T3-5	2.74	6.41	12.18	54.14	0.41	1.04	9.49	1.13	0.21	10.39	98.13
RF19 -T4-1	3.27	3.06	12.32	54.28	0.40	0.96	9.31	1.26	0.21	11.52	96.60
RF19 -T4-2	2.81	5.87	11.60	53.31	0.39	0.55	10.76	1.07	0.21	10.66	97.22
RF19 -T4-4	2.63	7.22	14.47	51.62	0.58	0.87	10.47	1.21	0.20	10.30	99.58
RF19 -T4-5	3.32	5.03	13.36	51.03	0.40	0.58	10.93	1.35	0.20	10.30	96.51
RF19 -T4-7	2.27	10.50	13.76	50.25	0.86	0.84	10.48	1.01	0.20	10.15	100.33

Using values from XRF measurements, a total alkali silica (TAS) diagram was plot for RF (figure 15). Error bars are not included for ease of interpretation. Maximum error for the plotted values of $Na_2O + K_2O$ is ± 0.61 weight percent and the maximum error for SiO_2 is ± 2.97 weight percent. The range of XRF values in figure 15 show that RF plots within the basalt and basaltic andesite. Values are averages of each sample in figure 15.
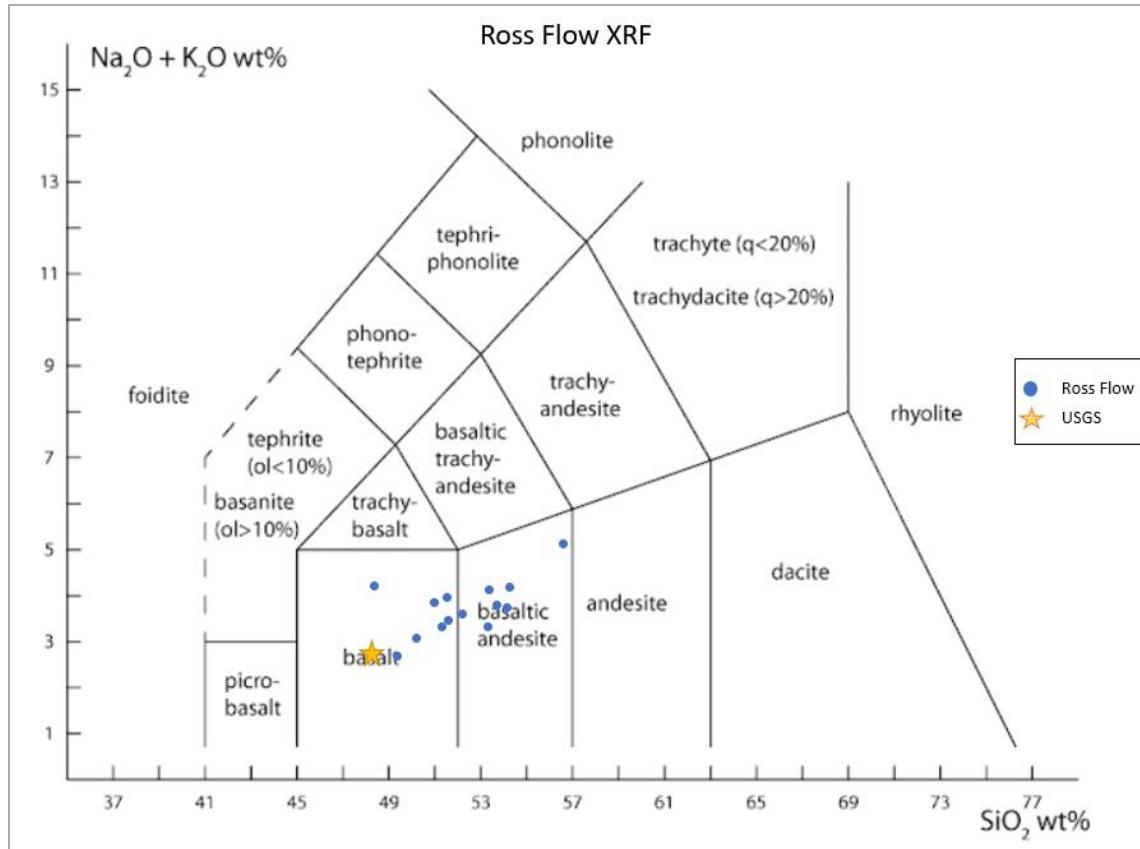
Figure 15: TAS diagram for RF using values from XRF in-situ measurements.

Harker diagrams were plotted using table 8 and error bars are 1 sigma calculated using standard deviation in figure 16. Errors on certain points are not visible due to their small value. Samples RF19-T4-1, and RF19-T4-2 have average error bars of all XRF 1 sigma error values as only one measurement was usable within the 95% to 105% total range. The silica range of RF is between 48.44 and 56.61 weight percent from the XRF values. NaO_2 ranges between 2.27 and 3.81 wt. % and MgO is between 3.06 and 10.50 wt. %. Al_2O_3 wt. % ranges between 7.59 and 16.90 and P_2O_5 has a range of 0.23 and 1.36 wt. %. K_2O ranges between 0.41 and 1.54 wt. % and CaO wt. % has a range of 7.37 and 10.93. The range of TiO_2 is 0.49 to 1.35 wt. % and FeO has a range between 9.64 and 12.67 wt. %. The ranges of these values can be seen in figure 16 with the star denoting the lab measured USGS sample from Ross Flow (Donnelly-Nolan 1993).
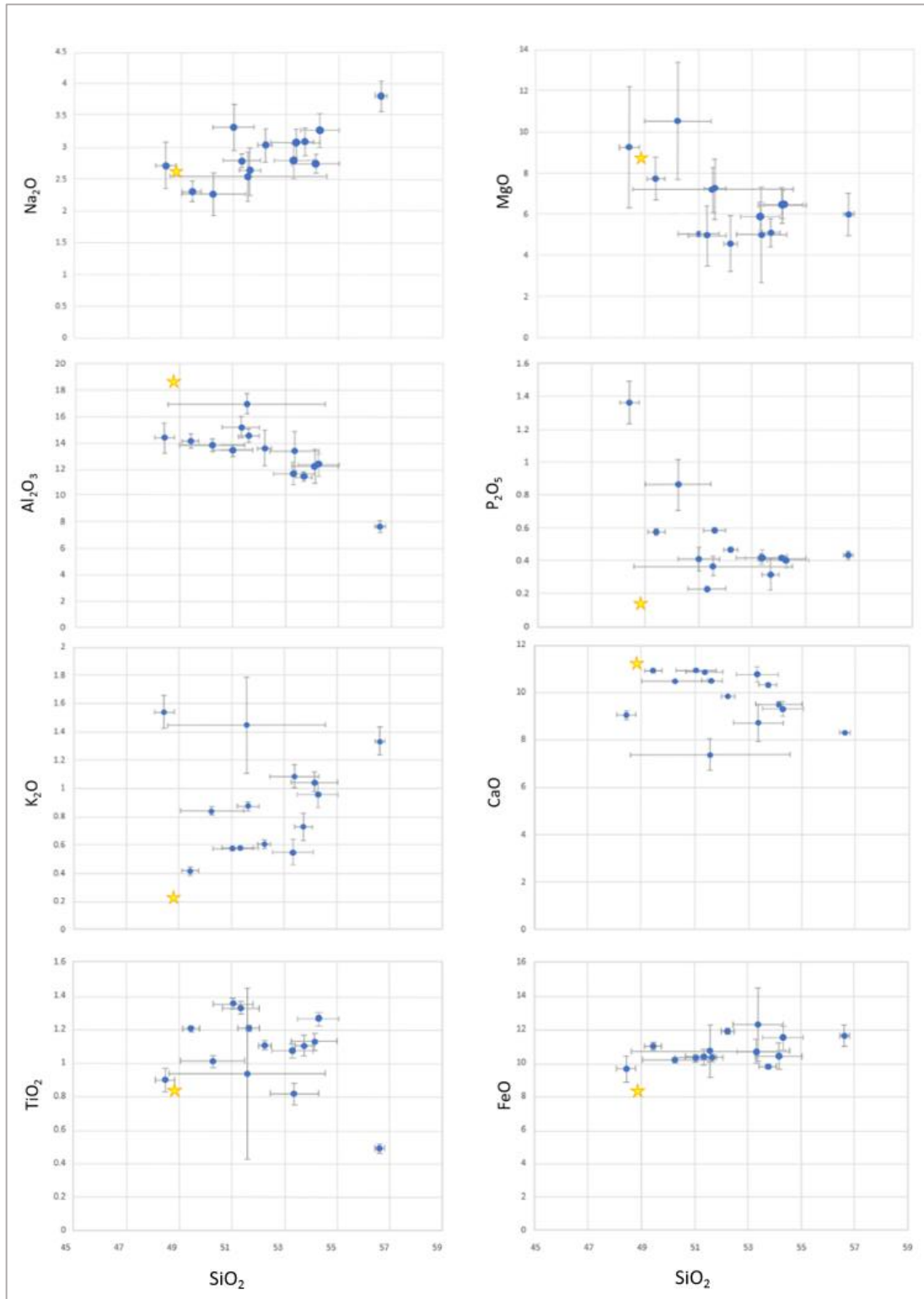
Figure 13: XRF Harker Diagrams. Blue dots are samples with bars signifying a 1 sigma error. The star is a USGS database sample tested with an XRF for comparison (Donnelly-Nolan 1993).

3.4 Crystallinity

The crystallinity of the two lava flows is shown in figure 17 made using table 9. Five samples were used for RF with two samples of surface, two of vent, and one of margin categories. There is no rootless cone crystallinity at RF due to rootless cones not being present at the lava flow. The highest crystallinity at RF is the surface with 19.84 % average crystallinity. Note that RF19-T4-9 is not included in these values due to field complications, but as evident in figure 10 the sample is highly crystalline.

Vent and rootless cone categories for BD each represent a single sample, respectively. The margin category of BD represents an average of two samples and the surface category of BD represents three samples. The highest crystallinity at BD is BD19-07-S1, a vent sample, with a dendritic crystalline matrix (figure 9) and the lowest crystallinity is from the rootless cone sample.

Table 9: Average crystallinity of BD and RF according to category

Category	Blue Dragon Crystallinity %	Ross Flow Crystallinity %
Margin	21.60	16.66
Surface	17.89	19.84
Vent	74.11	15.41
Rootless Cone	9.41	N/A
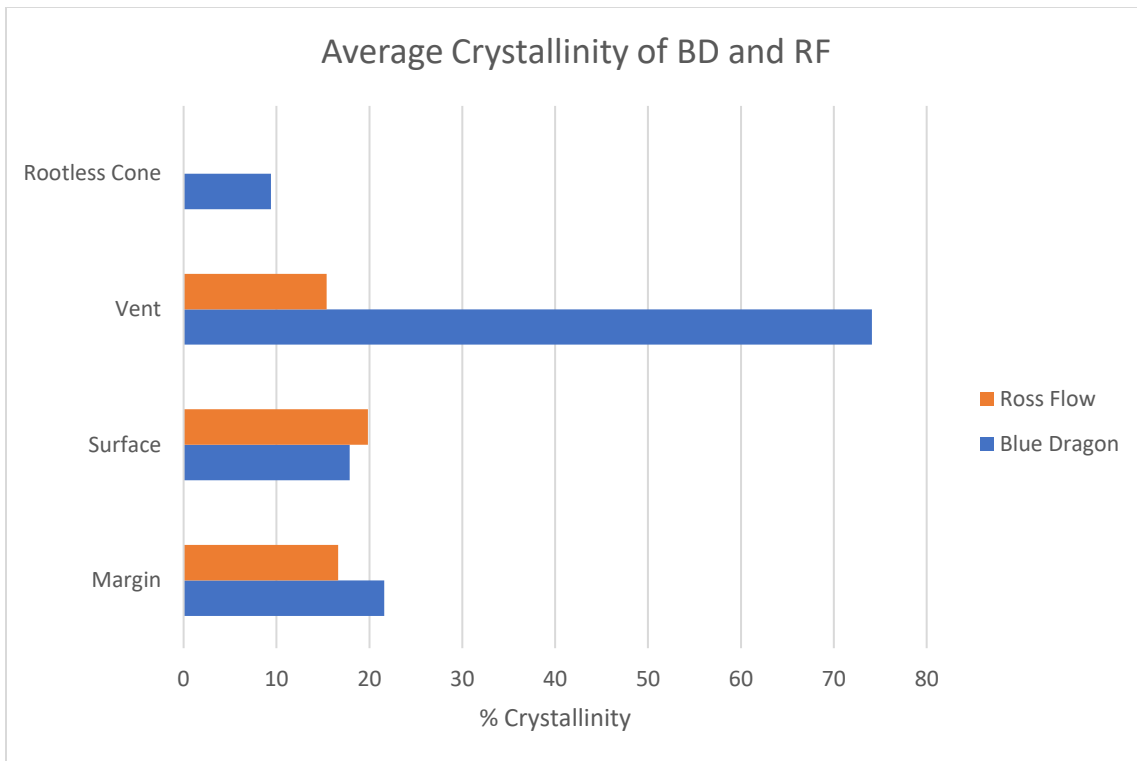
Figure 17: Average crystallinity for both RF and BD according to category.

Crystallinity values in figure 18 are plot against average reflectance with an error of 1 sigma calculated from the standard deviation of both crystallinity and reflectance, respectively. Crystallinity in BD ranged from 9.4% to 74.1% between the different categories. Surface crystallinity has values of 13.4%, 18.2%, and 22.1%. Margin crystallinity values are 18.5% and 24.7%The outlier of BD19-07-S1, a vent sample, with crystallinity 74.1% exhibit dendritic oxide crystals that permeate through the sample. Without the outlier, crystallinity of BD remains below 30%. The lowest crystallinity at BD is 9.4 % and the lowest crystallinity at RF is 12.2%. RF crystallinity ranges between 12.2% to 20.9%. The margin of RF has a crystallinity value of 16.6%. The surface category of RF has crystallinity values of 18.8% and 20.9%. Vent samples of RF contain crystallinity percents of 12.2% and 18.6%. The lowest calculated crystallinity of each flow respectively has the lowest average reflectance according to flow.
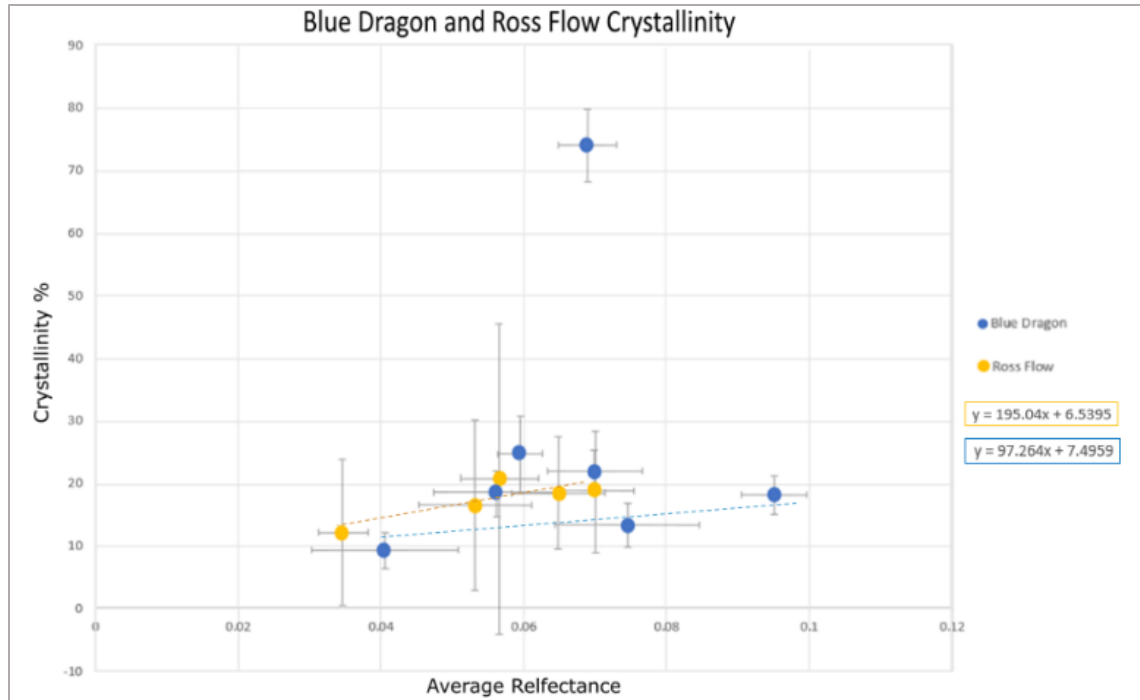
Figure 1814: Crystallinity of BD and RF plot against the average reflectance

The slopes of RF and BD in figure 18 use the average crystallinities for the equations. The equation of slope for BD excludes the dendritic crystalline sample BD19-07-S1 with the crystallinity percent of 74.1. The slopes are positive for both BD and RF illustrating a positive correlation between crystallinity percentage and average reflectance.

Part 4: Discussion

4.1 Mineralogic Impact

Both BD and RF are basaltic lava flows, but as stated before they are two very different lava flows. Mineralogically both lava flows contain olivine, plagioclase, and augite, but BD also contains titanian oxides and apatite. The range of oxides and apatite through the samples of BD, typically >1%-3% oxides and >1%-2% apatite, does not increase the reflectance with increased percentages of these minerals. Looking at three samples from the Blue Dragon, BD19-19-S1, BD19-15-S3, and BD19-12-S2 illustrates this. BD19-19-S1 has an average reflectance of 0.059 and an average crystallinity of 24.75%. This sample has an average oxide percent of 2.17 and average apatite percent of 0.81. BD19-15-S3 has the highest reflectance of the BD samples at 0.095 and a lower average crystallinity than BD19-19-S1 (figure 18). The average oxide percentage of BD19-15-S3 is 0.79 and the average apatite percentage is 0.37. The BD sample with the lowest reflectance, 0.041, is BD19-12-S2 and an average crystallinity of 9.41%. Oxide and apatite average percentages for BD19-12-S2 are 0.85% and 0.21% respectively. This shows that the changes of oxides or apatite between BD samples does not positively or negatively impact the reflectance.

The Blue Dragon lava flow is more mineralogically complex, with apatite, titanian oxides, plagioclase, and olivine, than the Ross Flow which predominately only has phenocrysts of olivine and plagioclase. Yet, despite these mineralogic differences between RF and BD, apart from BD19-07-S1, they both show a positive trend in figure 18. The R^2 value of the RF trendline is 0.659 and fits well with the data. The BD R^2 value is 0.137 a less fit than the RF R^2 value denoting a larger spread in the data. This may be due to the differences between RF and BD. RF is a mineralogically simple flow and has large phenocrysts of olivine and plagioclase set in its glassy matrix. The size of the RF phenocrysts causes the error of crystallinity to be larger than what is seen with BD. On the other hand, BD has phenocrysts of apatite, titanian oxides, plagioclase, and olivine. The error of crystallinity is smaller, due to the uniform size and distribution of phenocrysts through BD samples.

These two lava flows have many differences, yet as the crystallinity increases, so does the reflectance. In the case of BD this holds true with the exclusion of BD19-07-S1. The sample BD19-07-S1 contains dendritic microlites, which may decrease the reflectance of the sample. Weitz and Head III 1999 looked at ultraviolet spectra of the Marius Hills Plateau of the moon and found that microlites in assumed lunar spatter features darkened the spectra. Ultra-violet visible spectra uses a shorter wavelength of 415-1000 nm and functions by emitting light at a sample, similar to VNIR (Weitz and Head III 1999, Heather et al. 2003). Ultra-violet visible spectroscopy has been used to identify minerals and oxide signatures of lunar basalts by analyzing reflectance and absorbance features (Staid and Pieters 2001, Sato et al. 2017). I theorize that if interference of microlitic or dendritic textures are darkening the spectra in the VNIR wavelength range as it did in the ultra-violet range, according to Weitz and Head III 1999, then the lower reflectance of sample BD19-07-S1 is due to the dendritic microlite texture.

Excluding the dendritic sample in BD, as crystallinity increases reflectance increases as well. While the equation of the trendlines is not the same between the RF and BD, they both exhibit a positive relationship between crystallinity and reflectance. Dendritic and microlitic samples have been shown to influence ultra-violet spectra and may have a similar effect in the VNIR spectrum.

4.2 VNIR Spectral Interpretation

In figures 12, 13, and 14 there are VNIR spectra grouped and averaged together. Absorbance features are marked and possible minerals are associated with them. According to Hunt et al. 1974 basalts are relatively spectrally featureless, which can be seen clearly in figure 10 with BD's surface and margin spectra lines, but with RF and the rootless cone/ vent spectra of BD this is not the case. There are clear absorbance features and differences in slope within the spectra. Absorbance features can be explained through the elemental composition of each mineral and the possible hydration within them. The increase in slope found in VNIR spectra of RF can be associated with dust and windfall pumice found in the area. The absorbance features

marked in figures 12,13, and 14 are attributed to minerals with the same absorbance features in their spectra. The two spectral lines of weathered 1 and 2 at RF were excluded from identifying absorbance features due to the increased reflectance and/or different spectral shape. It is likely that these areas on RF were coated with dust or other microscopic material which was read. Dust and other environmental coatings impact the VNIR spectra at RF. Choosing clean and visibly dust free and unweathered surfaces will ensure clean spectra that exhibits absorbance features of the minerals within the lava.

4.3 The Margin to the Vent

The assumptions made by categorizing the lava flows into vent, margin, surface, and rootless cone are related to the cooling rate and the time of crystallization (Winter 2010, Griffiths 2000). Margin is the furthest from the vent and the lava would have the time it traveled to its emplacement to grow phenocrysts so long as the temperature required for growth was sustained (Crisp et al. 1994, Cashman et al. 1999, Griffiths 2000). Thus, margin is assumed to have the highest crystal percentage and highest average reflectance. In figure 19 RF follows this assumption. The surface is the intermediary between the vent and margin, thus would have experienced a higher temperature gradient than the margin and cooled to cease movement and crystal growth. Surface is assumed to have an average reflectance associated with higher crystallinity than the vent samples. In figure 19 BD does not exhibit a trend between distance from the vent and reflectance.
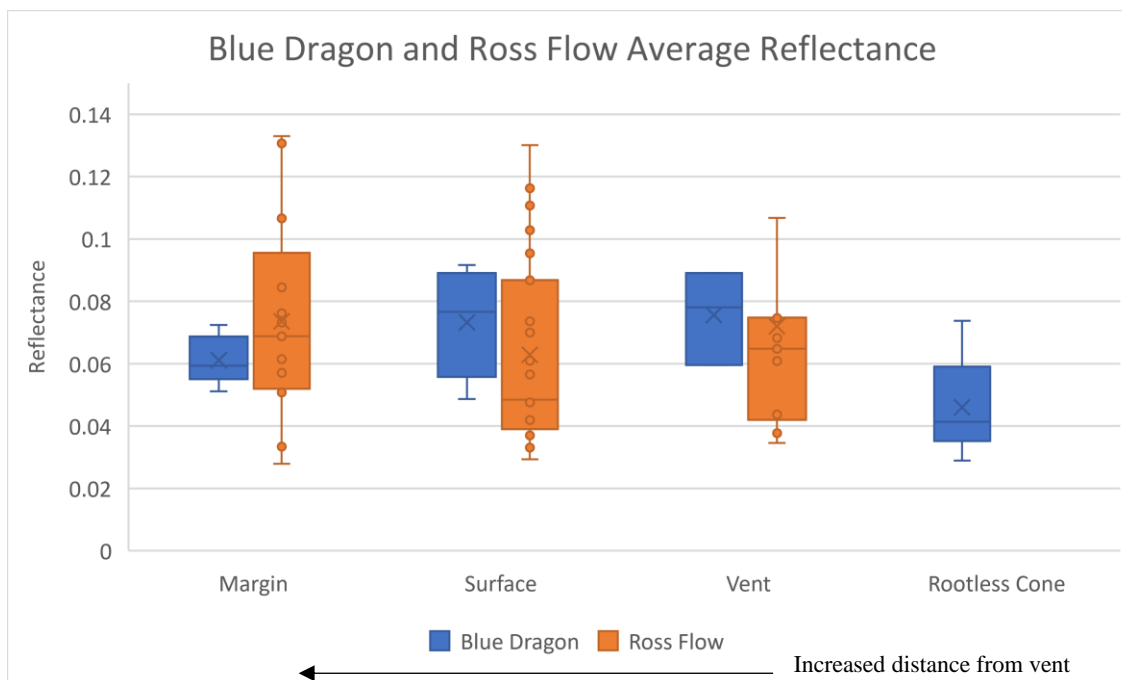
Figure 19: Box and Whisker plot of RF and BD using average reflectance. Error is set to 1 sigma.

One large difference between RF and BD is how the lava flow formed and the volume of lava erupted over time. RF appears to have been a short-lived lava flow that created the simple 1 km long RF. BD on the other hand is a complex series of lava tubes which fed the expansive flow when it was active. If the insulation of the lava tubes during transport impacts the growth rate of the crystals within the molten lava, then the lower crystallinity at the margin of BD as seen in figure 19, begins to make sense. In addition, the rootless cone category of BD are vent-like features erupted from the lava tubes onto the surface. Thus, they were originally formed from the insulated lava and cooled quickly enough to retain a low crystallinity and average reflectance. I predict that with simple lava flows like RF, there will be a trend of increasing reflectance with increasing distance from the vent. For more complex lava flows like BD, I predict that the vent and surface areas will have the highest reflectance as margins and rootless cones are fed from lava tubes.

4.4 Ross Flow and XRF

Geochemistry data from the XRF is plotted as Harker diagrams in figure 16 with the yellow star being the measured USGS XRF values for RF (Donnelly-Nolan 1993).

No XRF data was found from BD as it was not saved to the instrument in the field and was irretrievable. There is variance in the XRF values of RF and the USGS sample is less silicic than the field measured XRF values. Sehlke et al. 2019 examined the effect surface roughness had on the XRF instruments. The surface roughness refracts and reflects the beam impacting the measurement of the XRF (Sehlke et al. 2019, Rader et al. 2020). It is likely that the surface roughness of RF played a role in skewing the data presented in figure 16. The Harker diagrams have the major oxides plot against SiO_2. These plots can decode the crystallization history of RF. Looking at MgO, associated with olivine, and Al_2O_3 associated with plagioclase the decreasing trend with increasing silica shows that these minerals were crystallizing and depleting the melt. Yet, FeO stands out as it has a slight increase with increasing SiO_2. FeO is associated with olivine and should exhibit a decreasing trend with increased SiO_2. Thus, I assume that the surface roughness has negatively impacted the measured geochemistry data as it is predominately more silicic than the USGS sample and the FeO increase is incorrect.

4.5 Project Goal

The goal of this project is to determine if there is a relationship between reflectance and crystallinity. To determine if this was true, we used VNIR on two selected lava flows with specific differences and similarities. Both the RF and BD are considered basaltic pahoehoe flows, but beyond this they are quite different. BD is much larger than the 1 km long RF and the samples and data collected were only from phase 1 of the lava flow (Chadwick et al. 2019). Besides a dramatic difference in size, there is also the crystallinity of the two lava flows that reflects in figures 14 and 15. BD has apatite and oxides that RF does not have and the phenocrysts in BD are often smaller than those found in RF. Traverses were used in RF, giving a more complete profile of the lava flow from edge to edge, but BD was far too big to complete traverses over the area we sampled in only a day and half.

The categories of margin, surface, rootless cone, and vent have assumptions of their cooling history, but with BD the distance from the vent does not equate to

increased reflectance. BD shows that the highest average reflectance occurs at the surface and not at the margins. This may be attributed to the presence of lava tubes that transported the once molten lava to its current emplacement. While the lava was traveling in the tubes it was insulated from the outside conditions and therefore the growth of the crystals was slowed (Keszthelyi 1995, Winter 2010). The surface has the highest reflectance on BD with the vent following closely behind. Yet, the margin is lower than the vent samples and surface samples. Herein lies the issue of categorizing both RF and BD the same. For BD, the assumption that the crystallinity, and thus the reflectance, will be the greatest at the margin is incorrect. I attribute this to the complexity of the lava flow with the intertwining of lava tubes.

4.6 Implications for the Future

Crystallinity and reflectance have been shown to have a positive relationship in both RF and BD. Applying this technique to more basaltic lava flows can increase our ability to recognize differing basalt signatures that do not resemble the typical flat glassy spectra of basalt (Hunt et al. 1974). VNIR is a technique that can be modified for use by a drone or satellite and opens the realm of analyzing difficult to reach or dangerous areas. Active lava flows are hazardous to humans, thus a drone using this technique can gain an estimate of crystallinity. Satellites can be used in places such as Antarctica where reaching lava flows is arduous and treacherous.

Applying this knowledge to future questions, projects or missions, a simple relationship between crystallinity and reflectance can be drawn. This aids in identifying a single variable in the problem of viscosity and possibly offering a new way to identify rock types using VNIR from satellites or drones when the area is not accessible to human traffic.

4.7 BD and RF vs 2021 Iceland Eruption

The Fagradalsfjall eruption in Iceland in March of 2021 and provides a look at how a larger lava flow like BD behaves versus a simple lava flow like RF. (Reykjanes

Peninsula 2021). In addition, from watching the live feeds provided of the volcano many insights can be drawn and applied to both BD and RF.

During the 2021 Fagradalsfjall eruption, fissures opened March 19, 2021 and began erupting spatter and building ramparts before they evolved into conical vent features over the span of days (Global Volcanism Program 2021). The building of the spatter ramparts resembled the RF chimneys (figure 4). Using the Iceland fissure eruptions as an analog for how RF would have behaved during its own eruption it is likely that the duration of the RF eruption was over the span of hours to days depending on the rate of eruption. Had Fagradalsfjall stopped erupting a few days after it began, the cooling history would resemble that of RF. If the cooling history were the same as RF, then the crystallinity and reflectance would resemble RF as well.

Like BD, the Fagradalsfjall eruption also exhibits lava tubes which feed the margin and the surface (Global Volcanism Program 2013). As the eruption advanced lava tubes at Fagradalsfjall formed and fed the farther reaches of the lava flow (Reykjanes Peninsula 2021). Lava is fed through lava tubes, but it also flows over the surface or in channels which may not reach the margin of the flow (Reykjanes Peninsula 2021). Thus, though the margin is the furthest from the vent, it is likely in a complex lava flow that the surface is one of the last areas to cool. The insulation from travelling through the lava tubes and having a greater temperature from the margin, the surface can present with a higher crystallinity and increased reflectance. This is visible in figure 18 as the surface reflectance is higher than those of the margin the area assumed to have highest crystallinity. Therefore, I predict that the reflectance of Fagradalsfjall will resemble that of BD where the vent or surface will have the highest reflectance.

Part 5: Conclusion

In 2019 the IceCrystal team set out to use VNIR, and XRF field instruments on lava flows in the Northwest to identify any relationships between crystallinity and reflectance. Two of those flows are the Blue Dragon lava flow and the Ross Flow. Two basaltic lava flows with differing characteristics, which proved useful in exploring absorbance features and assumptions which had been made prior.

The findings thus far are as follows:

1.   In the case of BD and RF as crystallinity increase average reflectance increases as well. When glass increases, average reflectance is seen to decrease.

2.   With increased distance from the vent at RF crystallinity increases as does average reflectance. At simple lava flows like RF this trend should be present.

3.   BD being a complex lava flow with lava tubes, does not show a relationship between increased distance from the vent and increased reflectance.

4.   Absorbance features found in VNIR spectra correlate to absorbances found in the minerals present at each respective lava flow.

5.   The complexity of the lava flow plays a part in the distribution of crystallinity. At RF, increased distance from the vent average reflectance also increases. The complexity of BD with its interwoven lava tubes and size is seen to deviate from what is seen at RF. Lava tubes play a role in how crystallinity is distributed throughout complex lava flows due to its insulating effects.

6.   Microlites can darken spectra in ultra-violet spectroscopy and may do the same in VNIR. In sample BD19-07-S1, the dendritic and microlitic texture may decrease the reflectance.

7.   Changes in crystallinity percentages of oxides and apatite in BD does not significantly alter the average reflectance.

8.   The 2021 eruption at Fagradalsfjall appears to be a similarly complex lava flow to BD. Thus, the Fargradalsfjall eruption should produce similar trends in reflectance to BD.

9.   In-situ measurements of XRF are impacted by the surface roughness and distinguishing between basalt and basaltic-andesite is unlikely, differentiating between basalt and andesite is possible.

Future work should focus on the applicability of this technique on other lava flows on earth and determine its usefulness for extraterrestrial exploration as well as hazard management. This should be tested on active lava flows to determine the impact thermal has on the measuring of crystallinity and determine if it is still useable as a hazard management tool for defining a parameter of viscosity.

References

Angelis, S. D., Sanctis, M. C. D., Ammannito, E., Carli, C., Iorio, T. D., Frigeri, A., &
Manzari, P. (2014). VNIR spectral measurements on rock slabs with ExoMars-
Ma_Miss instrument. *European Planetary Science Congress,* Vol. (9), 2.

Black, S.R., Yingst, R. A., & Hynek, B. M., (2016). Field-Portable VNIR Spectrometry:
Applications for Mars Rover Operational Strategies Testing at Terrestrial Analog
Sites. *Spectroscopy*, 29-35.

Bost, N., Westall, F., Gaillard, F., Ramboz, C., & Foucher, F. (2012). Synthesis of a
spinifex-textured basalt as an analog to Gusev crater basalts, Mars: Artificial
Martian basalt. *Meteoritics & Planetary Science*, Vol. (47), 820–831. Doi:
10.1111/j.1945-5100.2012.01355

Butcher, G. (2016). *Tour of the electromagnetic spectrum* (Third edition). National
Aeronautics and Space Administration.

Cannon, K. M., J. F. Mustard, S. W. Parman, E. C. Sklute, M. D. Dyar, and R. F. Cooper
(2017), Spectral properties of Martian and other planetary glasses and their
detection in remotely sensed data. *Journal of Geophysical Research: Planets*, Vol.
(122), 249–268. Doi:10.1002/2016JE005219

Carli, C. (2009). Spectral analyses in the vnir of igneous rocks: surface composition
characterization of terrestrial planets. *Plinius,* n. 35, 83-90.

Carli, C., Serventi, G., & Sgavetti, M. (2015). VNIR spectral characteristics of terrestrial
igneous effusive rocks: Mineralogical composition and the influence of texture.
Geological Society of London, n. 401,139–158. Doi: 10.1144/SP401.19

Carli, C., Roush, T. L., Pedrazzi, G., & Capaccioni, F. (2016). Visible and Near-Infrared
(VNIR) reflectance spectroscopy of glassy igneous material: Spectral variation,
retrieving optical constants and particle sizes by Hapke model. *Icarus*, Vol. (266),
267–278. https://doi.org/10.1016/j.icarus.2015.10.032

Carli, C., Pratesi, G., Moggi-Cecchi, V., Zambon, F., Capaccioni, F., & Santoro, S. (2018).
Northwest Africa 6232: Visible-near infrared reflectance spectra variability of an

olivine diogenite. *Meteoritics & Planetary Science*, Vol. (53), 2228–2242. Doi: 10.1111/maps.13056

Cashman, K. V., Thornber, C., & Kauahikaua, J. P. (1999). Cooling and crystallization of lava in open channels, and the transition of Pāhoehoe Lava to ʼAʼā. *Bulletin of Volcanology*, Vol. (61), 306–323. https://doi.org/10.1007/s004450050299

Chadwick, J., Schwartz, M., Mclane, D., Collins, E., & Kamenov, G. (2019). Compositional heterogeneity of the 3.4 km3 Blue Dragon flow, Craters of the Moon Volcanic Field, Idaho. *Journal of Volcanology and Geothermal Research*, Vol. (388), 114. https://doi.org/10.1016/j.jvolgeores.2019.106690

Crisp, J., Cashman, K., Bonini, J.A., Hougen, S., & Pieri, D. (1994). Crystallization history of the 1984 Mauna Loa lava flow. *Journal of Geophysical Research*, Vol. (99), 7177-7198.

Diniega, S., Smrekar, S. E., Anderson, S., & Stofan, E. R. (2013). The influence of temperature-dependent viscosity on lava flow dynamics: thermo-viscous lava flow dynamics. *Journal of Geophysical Research: Earth Surface*, Vol. (118), 1516–1532. https://doi.org/10.1002/jgrf.20111

Donaldson, C. H., (1974). Olivine Crystal Types in Harrisitic Rocks of the Rhum Pluton and in Archean Spinifex Rocks. *Geological Society of America Bulletin,* Vol. (85), 1721-1726.

Donnelly-Nolan, J. M., Champion, D. E., Miller, C. D., Grove, T. L., & Trimble, D. A. (1990). Post-11,000-year volcanism at Medicine Lake Volcano, Cascade Range, northern California. *Journal of Geophysical Research*, Vol. (95), 19693-19704. https://doi.org/10.1029/JB095iB12p19693

Donnelly-Nolan, J.M., Nathenson, M., Champion, D.E., Ramsey, D.W., Lowenstern, J.B., Ewert, J.W., 2007. Volcano hazards assessment for Medicine Lake volcano, northern California. U.S. Geol. Survey. Scientific Investigation Report. 2007-5174-A, 26 [http://pubs.usgs.gov/sir/2007/5174/a/]

Donnelly-Nolan, Julie M., 1993, NGDB rock sample M202958: U.S. Geological Survey
database, accessed June 6, 2021, at https://mrdata.usgs.gov/ngdb/rock/show-
ngdbrock.php?lab_id=M202958

Fagents, S. A., & Thordarson, T. (2007). Rootless volcanic cones in Iceland and on Mars.
The Geology of Mars: Evidence from Earth Based Analog, (pp. 151–177).
https://doi.org/10.1017/CBO9780511536014.007

Gansecki, C., Lee, R. L., Shea, T., Lundblad, S. P., Hon, K., & Parcheta, C. (2019). The
tangled tale of Kīlauea's 2018 eruption as told by geochemical monitoring.
Science, Vol. (366), 9, eaaz0147. https://doi.org/10.1126/science.aaz0147

Griffiths, R. W. (2000). The Dynamics of Lava Flows. *Annual Review of Fluid Mechanics*,
Vol. (32), 477–518. https://doi.org/10.1146/annurev.fluid.32.1.477

Greeley, R. (2005). Fluid lava flows in Gusev crater, Mars. *Journal of Geophysical
Research*, Vol. (110), 6. https://doi.org/10.1029/2005JE002401

Global Volcanism Program, 2013. Krysuvik-Trolladyngja (371030) in Volcanoes of the
World, v. 4.10.1 (29 Jun 2021). Venzke, E (ed.). Smithsonian Institution.
Downloaded 20 Jul 2021 (https://volcano.si.edu/volcano.cfm?vn=371030).
https://doi.org/10.5479/si.GVP.VOTW4-2013

Global Volcanism Program, (2021). Report on Krysuvik-Trolladyngja (Iceland). In:
Sennert, S K (ed.), Weekly Volcanic Activity Report, 17 March-23 March 2021.
Smithsonian Institution and US Geological Survey.

Harris, A. J. L., & Allen, J. S. (2008). One-, two- and three-phase viscosity treatments for
basaltic lava flows. *Journal of Geophysical Research*, Vol. (113), 15.
https://doi.org/10.1029/2007JB005035

Heather, D. J. (2003). Volcanism on the Marius Hills plateau: Observational analyses
using Clementine multispectral data. Journal of Geophysical Research, Vol. (108),
16. https://doi.org/10.1029/2002JE001938

Hunt, G.R.; Salisbury, J.W.; Lenhoff, C.J. (1974). Visible and near infrared spectra of

    minerals and rocks: IX. Basic and ultrabasic igneous rocks. *Modern Geology*. Vol.

    5, 15–22

Keszthelyi, L. (1995). A preliminary thermal budget for lava tubes on the Earth and

    planets. *Journal of Geophysical Research: Solid Earth*, Vol. (100), 20411–20420.

    https://doi.org/10.1029/95JB01965

Kokaly, R.F., Clark, R.N., Swayze, G.A., Livo, K.E., Hoefen, T.M., Pearson, N.C., Wise, R.A.,

    Benzel, W.M., Lowers, H.A., Driscoll, R.L., and Klein, A.J., (2017), *USGS Spectral*

    Library, Version 7: U.S. Geological Survey Data Series 1035, 61 p.,

    https://doi.org/10.3133/ds1035.

McClinton, J. T., White, S. M., Colman, A., Rubin, K. H., & Sinton, J. M. (2014). The role of

    crystallinity and viscosity in the formation of submarine lava flow morphology.

    Bulletin of Volcanology, Vol. (76), 13. Doi: 10.1007/s00445-014-0854-2

Pour, A. B., Park, Y., Park, T.-Y. S., Hong, J. K., Hashim, M., Woo, J., & Ayoobi, I. (2018).

    Regional geology mapping using satellite-based remote sensing approach in

    Northern Victoria Land, Antarctica. *Polar Science*, Vol. (16), 23–46.

    https://doi.org/10.1016/j.polar.2018.02.004

Reykjanes Peninsula, Iceland, eruption 2021: eruption and activity updates in live blog

    style. (2021). *Volcano Discovery*.

    https://www.volcanodiscovery.com/reykjanes/crisis2021/current-activity.html.

Rader, E., Sehlke, A., Ackiss, S. E., Reeder, A., Odegaard, K. A., Cerna, K., (2020), Can

    scatter of in-situ geochemical data be diagnostic for morphological and

    petrological features on lava surfaces?, Abstract [P063-15] Presented at 2020

    Fall Meeting, AGU, Washington, 15 Dec.

Rowan, L. C., Hook, S. J., & Abrams, M. J. (2003) Mapping Hydrothermally Altered Rocks

    at Cuprite, Nevada, Using the Advanced Spaceborne Thermal Emission and

Reflection Radiometer (Aster), A New Satellite-Imaging System. *Economic Geology,* Vol. (98), 1019-1027.

Sahagian, D. (1985). Bubble Migration and Coalescence during the Solidification of Basaltic Lava Flows. *The Journal of Geology*, Vol. (93), 205–211. https://doi.org/10.1086/628942

Sanchez, J. A., Reddy, V., Kelley, M. S., Cloutis, E. A., Bottke, W. F., Nesvorný, D., Lucas, M. P., Hardersen, P. S., Gaffey, M. J., Abell, P. A., & Corre, L. L. (2014). Olivine-dominated asteroids: Mineralogy and origin. *Icarus*, Vol. (228), 288–300. https://doi.org/10.1016/j.icarus.2013.10.006

Sato, H., Robinson, M. S., Lawrence, S. J., Denevi, B. W., Hapke, B., Jolliff, B. L., & Hiesinger, H. (2017). Lunar mare TiO 2 abundances estimated from UV/Vis reflectance. *Icarus*, Vol. (296), 216–238. https://doi.org/10.1016/j.icarus.2017.06.013

Scudder, N. A. (2021). The effects of magmatic evolution, crystallinity, and microtexture on the visible/near-infrared and thermal-infrared spectra of volcanic rocks. Icarus, Vol. (359), 27.

Sehlke, A., Mirmalek, Z., Burtt, D., Haberle, C. W., Santiago-Materese, D., Kobs Nawotniak, S. E., Hughes, S. S., Garry, W. B., Bramall, N., Brown, A. J., Heldmann, J. L., & Lim, D. S. S. (2019). Requirements for Portable Instrument Suites during Human Scientific Exploration of Mars. *Astrobiology*, Vol. (19), 401–425. https://doi.org/10.1089/ast.2018.1841

Serventi, G., Carli, C., Sgavetti, M., Ciarniello, M., Capaccioni, F., & Pedrazzi, G. (2013). Spectral variability of plagioclase–mafic mixtures (1): Effects of chemistry and modal abundance in reflectance spectra of rocks and mineral mixtures. *Icarus*, Vol. (226), 282–298. https://doi.org/10.1016/j.icarus.2013.05.041

Shea, T., Houghton, B. F., Gurioli, L., Cashman, K. V., Hammer, J. E., & Hobden, B. J. (2010). Textural studies of vesicles in volcanic rocks: An integrated

methodology. *Journal of Volcanology and Geothermal Research*, Vol. (190), 271–289. https://doi.org/10.1016/j.jvolgeores.2009.12.003

Sparks, R. S. J., & Pinkerton, H. (1978). Effect of degassing on rheology of basaltic lava. *Nature*, Vol. (276), 385–386. https://doi.org/10.1038/276385a0

Staid, M. I., & Pieters, C. M. (2001). Mineralogy of the last lunar basalts: Results from Clementine. *Journal of Geophysical Research: Planets*, Vol. (106), 27887–27900. https://doi.org/10.1029/2000JE001387

Stasiuk, M. V., Jaupart, C., & Sparks, R. S. J. (1993). Influence of cooling on lava-flow dynamics. *Geology*, Vol. 21, 335-338.

Turner, N. R., Perroy, R. L., & Hon, K. (2017). Lava flow hazard prediction and monitoring with UAS: A case study from the 2014–2015 Pāhoa lava flow crisis, Hawaiʻi. *Journal of Applied Volcanology*, Vol. (6), 11. Doi: 10.1186/s13617-017-0068-3

Vetere, F., Sato, H., Ishibashi, H., De Rosa, R., & Donato, P. (2013). Viscosity changes during crystallization of a shoshonitic magma: New insights on lava flow emplacement. *Journal of Mineralogical and Petrological Sciences*, Vol. (108), 144–160. https://doi.org/10.2465/jmps.120724

Winter, J. D., & Winter, J. D. (2010). Principles of igneous and metamorphic petrology. New York: Prentice Hall.

Appendix:

Table 1: digitized notebook of field observations, sample numbers, and instrument data numbers of the Blue Dragon Lava flow at Craters of the Moon National Monument and Preserve

Sample ID	Sample Number	Spot Number	Analysis Number	GPS_N	GPS_W	Collected	Category	Morphology	Keywords	Surface Roughness (mm)	Notes
BD19	1	S1	1	43.42347	113.5534	N	margin	spiney pahoehoe	-	-	-
BD19	1	S1	2	43.42347	113.5534	N	margin	spiney pahoehoe	-	-	-
BD19	1	S1	3	43.42347	113.5534	N	margin	spiney pahoehoe	-	-	-
BD19	1	S2	1	43.42347	113.5534	N	margin	spiney pahoehoe	-	-	-
BD19	1	S2	2	43.42347	113.5534	N	margin	spiney pahoehoe	-	-	-
BD19	1	S2	3	43.42347	113.5534	N	margin	spiney pahoehoe	-	-	-
BD19	1	S3	1	43.42347	113.5534	N	margin	spiney pahoehoe	-	-	-
BD19	1	S3	2	43.42347	113.5534	N	margin	spiney pahoehoe	-	-	-
BD19	1	S3	3	43.42347	113.5534	N	margin	spiney pahoehoe	-	-	-
BD19	2	S1	1	43.4233	113.55328	N	margin	spiney pahoehoe	blue	-	-
BD19	2	S1	2	43.4233	113.55328	N	margin	spiney pahoehoe	blue	-	-

BD19	2	S1	3	43.4233	113.55328	N	margin	spiney pahoehoe	blue	-	-
BD19	2	S2	1	43.4233	113.55328	N	margin	spiney pahoehoe	blue	-	-
BD19	2	S2	2	43.4233	113.55328	N	margin	spiney pahoehoe	blue	-	-
BD19	2	S2	3	43.4233	113.55328	N	margin	spiney pahoehoe	blue	-	-
BD19	2	S3	1	43.4233	113.55328	N	margin	spiney pahoehoe	blue	-	-
BD19	2	S3	2	43.4233	113.55328	N	margin	spiney pahoehoe	blue	-	-
BD19	2	S3	3	43.4233	113.55328	N	margin	spiney pahoehoe	blue	-	-
BD19	3	S1	1	43.42279	113.55388	N	margin	-	grey	-	-
BD19	3	S1	2	43.42279	113.55388	N	margin	-	grey	-	-
BD19	3	S1	3	43.42279	113.55388	N	margin	-	grey	-	-
BD19	3	S2	1	43.42279	113.55388	N	margin	-	grey	-	-
BD19	3	S2	2	43.42279	113.55388	N	margin	-	grey	-	-
BD19	3	S2	3	43.42279	113.55388	N	margin	-	grey	-	-
BD19	3	S3	1	43.42279	113.55388	N	margin	-	grey	-	-
BD19	3	S3	2	43.42279	113.55388	N	margin	-	grey	-	-
BD19	3	S3	3	43.42279	113.55388	N	margin	-	grey	-	-
BD19	4	S1	1	43.42271	113.55403	N	margin	pahoehoe	blue, smooth, breakout	<1	-
BD19	4	S1	2	43.42271	113.55403	N	margin	pahoehoe	blue, smooth, breakout	<1	-
BD19	4	S1	3	43.42271	113.55403	N	margin	pahoehoe	blue, smooth, breakout	<1	-

BD19	4	S2	1	43.42271	113.55403	N	margin	pahoehoe	blue, smooth, breakout	<1	-
BD19	4	S2	2	43.42271	113.55403	N	margin	pahoehoe	blue, smooth, breakout	<1	-
BD19	4	S2	3	43.42271	113.55403	N	margin	pahoehoe	blue, smooth, breakout	<1	-
BD19	4	S3	1	43.42271	113.55403	N	margin	pahoehoe	blue, smooth, breakout	<1	-
BD19	4	S3	2	43.42271	113.55403	N	margin	pahoehoe	blue, smooth, breakout	<1	-
BD19	4	S3	3	43.42271	113.55403	N	margin	pahoehoe	blue, smooth, breakout	<1	-
BD19	4	S4	1	43.42271	113.55403	Y	margin	pahoehoe	blue, smooth, breakout	<1	-
BD19	4	S4	2	43.42271	113.55403	Y	margin	pahoehoe	blue, smooth, breakout	<1	-
BD19	4	S4	3	43.42271	113.55403	Y	margin	pahoehoe	blue, smooth, breakout	<1	-
BD19	5	S1	1	43.42177	113.55734	N	hornito	spatter	black, glassy	-	-
BD19	5	S1	2	43.42177	113.55734	N	hornito	spatter	black, glassy	-	-
BD19	5	S1	3	43.42177	113.55734	N	hornito	spatter	black, glassy	-	-
BD19	5	S2	1	43.42177	113.55734	N	hornito	spatter	black, glassy	-	-
BD19	5	S2	2	43.42177	113.55734	N	hornito	spatter	black, glassy	-	-
BD19	5	S2	3	43.42177	113.55734	N	hornito	spatter	black, glassy	-	-
BD19	5	S3	1	43.42177	113.55734	N	hornito	spatter	black, glassy	-	-
BD19	5	S3	2	43.42177	113.55734	N	hornito	spatter	black, glassy	-	-
BD19	5	S3	3	43.42177	113.55734	N	hornito	spatter	black, glassy	-	-
BD19	6	S1	1	43.42173	113.5573	N	hornito	spatter	dry, reddish, glazed	1	-

BD19	6	S1	2	43.42173	113.5573	N	hornito	spatter	dry, reddish, glazed	1	-
BD19	6	S1	3	43.42173	113.5573	N	hornito	spatter	dry, reddish, glazed	1	-
BD19	6	S2	1	43.42173	113.5573	N	hornito	spatter	dry, reddish, glazed	1	-
BD19	6	S2	2	43.42173	113.5573	N	hornito	spatter	dry, reddish, glazed	1	-
BD19	6	S2	3	43.42173	113.5573	N	hornito	spatter	dry, reddish, glazed	1	-
BD19	6	S3	1	43.42173	113.5573	N	hornito	spatter	dry, reddish, glazed	1	-
BD19	6	S3	2	43.42173	113.5573	N	hornito	spatter	dry, reddish, glazed	1	-
BD19	6	S3	3	43.42173	113.5573	N	hornito	spatter	dry, reddish, glazed	1	-
BD19	7	S1	1	43.44084	113.55756	Y	vent	spatter	dark grey, dense, wringled, glazed	-	-
BD19	7	S1	2	43.44084	113.55756	Y	vent	spatter	dark grey, dense, wringled, glazed	-	-
BD19	7	S1	3	43.44084	113.55756	Y	vent	spatter	dark grey, dense, wringled, glazed	-	-
BD19	7	S2	1	43.44084	113.55756	N	vent	spatter	dark grey, dense,	-	-

									wringled, glazed		
BD19	7	S2	2	43.44084	113.55756	N	vent	spatter	dark grey, dense, wringled, glazed	-	-
BD19	7	S2	3	43.44084	113.55756	N	vent	spatter	dark grey, dense, wringled, glazed	-	-
BD19	7	S3	1	43.44084	113.55756	N	vent	spatter	dark grey, dense, wringled, glazed	-	-
BD19	7	S3	2	43.44084	113.55756	N	vent	spatter	dark grey, dense, wringled, glazed	-	-
BD19	7	S3	3	43.44084	113.55756	N	vent	spatter	dark grey, dense, wringled, glazed	-	-
BD19	8	S1	1	43.44084	113.55756	Y	vent	spatter	maroon	-	LIBS bad contact S1-S3
BD19	8	S1	2	43.44084	113.55756	Y	vent	spatter	maroon	-	LIBS bad contact S1-S3
BD19	8	S1	3	43.44084	113.55756	Y	vent	spatter	maroon	-	LIBS bad contact S1-S3

BD19	8	S2	1	43.44084	113.55756	N	vent	spatter	maroon	-	LIBS bad contact S1-S3
BD19	8	S2	2	43.44084	113.55756	N	vent	spatter	maroon	-	LIBS bad contact S1-S3
BD19	8	S2	3	43.44084	113.55756	N	vent	spatter	maroon	-	LIBS bad contact S1-S3
BD19	8	S3	1	43.44084	113.55756	N	vent	spatter	maroon	-	LIBS bad contact S1-S3
BD19	8	S3	2	43.44084	113.55756	N	vent	spatter	maroon	-	LIBS bad contact S1-S3
BD19	8	S3	3	43.44084	113.55756	N	vent	spatter	maroon	-	LIBS bad contact S1-S3
BD19	9	S1	1	43.44115	113.55757	N	vent	spatter	maroon, stretched vesicles	2	-
BD19	9	S1	2	43.44115	113.55757	N	vent	spatter	maroon, stretched vesicles	2	-
BD19	9	S1	3	43.44115	113.55757	N	vent	spatter	maroon, stretched vesicles	2	-
BD19	9	S2	1	43.44115	113.55757	N	vent	spatter	maroon, stretched vesicles	2	-

BD19	9	S2	2	43.44115	113.55757	N	vent	spatter	maroon, stretched vesicles	2	-
BD19	9	S2	3	43.44115	113.55757	N	vent	spatter	maroon, stretched vesicles	2	-
BD19	9	S3	1	43.44115	113.55757	N	vent	spatter	maroon, stretched vesicles	2	-
BD19	9	S3	2	43.44115	113.55757	N	vent	spatter	maroon, stretched vesicles	2	-
BD19	9	S3	3	43.44115	113.55757	N	vent	spatter	maroon, stretched vesicles	2	-
BD19	10	S1	1	43.44378	113.51901	N	surface	pahoehoe	blue, metallic	<1	-
BD19	10	S1	2	43.44378	113.51901	N	surface	pahoehoe	blue, metallic	<1	-
BD19	10	S1	3	43.44378	113.51901	N	surface	pahoehoe	blue, metallic	<1	-
BD19	10	S2	1	43.44378	113.51901	Y	surface	pahoehoe	blue, metallic	<1	-
BD19	10	S2	2	43.44378	113.51901	Y	surface	pahoehoe	blue, metallic	<1	-
BD19	10	S2	3	43.44378	113.51901	Y	surface	pahoehoe	blue, metallic	<1	-
BD19	10	S3	1	43.44378	113.51901	N	surface	pahoehoe	blue, metallic	<1	-
BD19	10	S3	2	43.44378	113.51901	N	surface	pahoehoe	blue, metallic	<1	-
BD19	10	S3	3	43.44378	113.51901	N	surface	pahoehoe	blue, metallic	<1	-
BD19	11	S1	1	43.44373	113.51897	Y	surface	pahoehoe	breakout, metallic, grey, purple, blue	-	See notes for depths

BD19	11	S1	2	43.44373	113.51897	Y	surface	pahoehoe	breakout, metallic, grey, purple, blue	-	See notes for depths
BD19	11	S1	3	43.44373	113.51897	Y	surface	pahoehoe	breakout, metallic, grey, purple, blue	-	See notes for depths
BD19	11	S2	1	43.44373	113.51897	Y	surface	pahoehoe	breakout, sky blue	-	See notes for depths
BD19	11	S2	2	43.44373	113.51897	Y	surface	pahoehoe	breakout, sky blue	-	See notes for depths
BD19	11	S2	3	43.44373	113.51897	Y	surface	pahoehoe	breakout, sky blue	-	See notes for depths
BD19	11	S3	1	43.44373	113.51897	N	surface	pahoehoe	breakout, dark purple, sky blue	-	See notes for depths
BD19	11	S3	2	43.44373	113.51897	N	surface	pahoehoe	breakout, dark purple, sky blue	-	See notes for depths
BD19	11	S3	3	43.44373	113.51897	N	surface	pahoehoe	breakout, dark purple, sky blue	-	See notes for depths
BD19	12	S1	1	43.44661	113.50637	N	hornito	spatter	stretched vesicles, reddish, glazed	2 to 3	
BD19	12	S1	2	43.44661	113.50637	N	hornito	spatter	stretched vesicles, reddish, glazed	2 to 3	

BD19	12	S1	3	43.44661	113.50637	N	hornito	spatter	stretched vesicles, reddish, glazed	2 to 3	
BD19	12	S2	1	43.44661	113.50637	Y	hornito	spatter	stretched vesicles, reddish	2 to 3	Uneven surfaces
BD19	12	S2	2	43.44661	113.50637	Y	hornito	spatter	stretched vesicles, reddish	2 to 3	Uneven surfaces
BD19	12	S2	3	43.44661	113.50637	Y	hornito	spatter	stretched vesicles, reddish	2 to 3	Uneven surfaces
BD19	12	S3	1	43.44661	113.50637	N	hornito	spatter	stretched vesicles, black	2 to 3	Uneven surfaces
BD19	12	S3	2	43.44661	113.50637	N	hornito	spatter	stretched vesicles, black	2 to 3	Uneven surfaces
BD19	12	S3	3	43.44661	113.50637	N	hornito	spatter	stretched vesicles, black	2 to 3	Uneven surfaces
BD19	13	S1	1	43.44668	113.50636	N	hornito	spatter	black	1	S3 shaky on LIBS
BD19	13	S1	2	43.44668	113.50636	N	hornito	spatter	black	1	S3 shaky on LIBS
BD19	13	S1	3	43.44668	113.50636	N	hornito	spatter	black	1	S3 shaky on LIBS
BD19	13	S2	1	43.44668	113.50636	Y	hornito	spatter	black	1	S3 shaky on LIBS

BD19	13	S2	2	43.44668	113.50636	Y	hornito	spatter	black	1	S3 shaky on LIBS
BD19	13	S2	3	43.44668	113.50636	Y	hornito	spatter	black	1	S3 shaky on LIBS
BD19	13	S3	1	43.44668	113.50636	N	hornito	spatter	black	1	S3 shaky on LIBS
BD19	13	S3	2	43.44668	113.50636	N	hornito	spatter	black	1	S3 shaky on LIBS
BD19	13	S3	3	43.44668	113.50636	N	hornito	spatter	black	1	S3 shaky on LIBS
BD19	14	S1	1	43.44664	113.50628	Y	hornito	spatter	black, glassy	2	
BD19	14	S1	2	43.44664	113.50628	Y	hornito	spatter	black, glassy	2	
BD19	14	S1	3	43.44664	113.50628	Y	hornito	spatter	black, glassy	2	
BD19	14	S2	1	43.44664	113.50628	N	hornito	spatter	black, glassy	2	
BD19	14	S2	2	43.44664	113.50628	N	hornito	spatter	black, glassy	2	
BD19	14	S2	3	43.44664	113.50628	N	hornito	spatter	black, glassy	2	
BD19	14	S3	1	43.44664	113.50628	N	hornito	spatter	black, glassy	2	
BD19	14	S3	2	43.44664	113.50628	N	hornito	spatter	black, glassy	2	
BD19	14	S3	3	43.44664	113.50628	N	hornito	spatter	black, glassy	2	
BD19	15	S1	1	43.44428	113.51534	Y	surface	spiney pahoehoe	inflated	5	
BD19	15	S1	2	43.44428	113.51534	Y	surface	spiney pahoehoe	inflated	5	
BD19	15	S1	3	43.44428	113.51534	Y	surface	spiney pahoehoe	inflated	5	
BD19	15	S2	1	43.44428	113.51534	N	surface	spiney pahoehoe	inflated	5	
BD19	15	S2	2	43.44428	113.51534	N	surface	spiney pahoehoe	inflated	5	

BD19	15	S2	3	43.44428	113.51534	N	surface	spiney pahoehoe	inflated	5	
BD19	15	S3	1	43.44428	113.51534	N	surface	spiney pahoehoe	inflated	5	
BD19	15	S3	2	43.44428	113.51534	N	surface	spiney pahoehoe	inflated	5	
BD19	15	S3	3	43.44428	113.51534	N	surface	spiney pahoehoe	inflated	5	
BD19	16	S1	1	43.4472	113.53402	N	surface	pahoehoe	metallic grey, striated, blue	<1	
BD19	16	S1	2	43.4472	113.53402	N	surface	pahoehoe	metallic grey, striated, blue	<1	
BD19	16	S1	3	43.4472	113.53402	N	surface	pahoehoe	metallic grey, striated, blue	<1	
BD19	16	S2	1	43.4472	113.53402	N	surface	pahoehoe	metallic grey, striated, blue	<1	
BD19	16	S2	2	43.4472	113.53402	N	surface	pahoehoe	metallic grey, striated, blue	<1	
BD19	16	S2	3	43.4472	113.53402	N	surface	pahoehoe	metallic grey, striated, blue	<1	
BD19	16	S3	1	43.4472	113.53402	Y	surface	pahoehoe	metallic grey, striated, blue	<1	
BD19	16	S3	2	43.4472	113.53402	Y	surface	pahoehoe	metallic grey, striated, blue	<1	
BD19	16	S3	3	43.4472	113.53402	Y	surface	pahoehoe	metallic grey, striated, blue	<1	
BD19	17	S1	1	43.44723	113.53405	N	surface	pahoehoe	sky blue	<1	
BD19	17	S1	2	43.44723	113.53405	N	surface	pahoehoe	sky blue	<1	
BD19	17	S1	3	43.44723	113.53405	N	surface	pahoehoe	sky blue	<1	
BD19	17	S2	1	43.44723	113.53405	N	surface	pahoehoe	sky blue	<1	

BD19	17	S2	2	43.44723	113.53405	N	surface	pahoehoe	sky blue	<1	
BD19	17	S2	3	43.44723	113.53405	N	surface	pahoehoe	sky blue	<1	
BD19	17	S3	1	43.44723	113.53405	Y	surface	pahoehoe	sky blue	<1	
BD19	17	S3	2	43.44723	113.53405	Y	surface	pahoehoe	sky blue	<1	
BD19	17	S3	3	43.44723	113.53405	Y	surface	pahoehoe	sky blue	<1	
BD19	18	S1	1	43.44744	113.53388	N	margin	spiney pahoehoe	inflated, black, glassy		2
BD19	18	S1	2	43.44744	113.53388	N	margin	spiney pahoehoe	inflated, black, glassy		2
BD19	18	S1	3	43.44744	113.53388	N	margin	spiney pahoehoe	inflated, black, glassy		2
BD19	18	S2	1	43.44744	113.53388	Y	margin	spiney pahoehoe	inflated, black, glassy		2
BD19	18	S2	2	43.44744	113.53388	Y	margin	spiney pahoehoe	inflated, black, glassy		2
BD19	18	S2	3	43.44744	113.53388	Y	margin	spiney pahoehoe	inflated, black, glassy		2
BD19	18	S3	1	43.44744	113.53388	N	margin	spiney pahoehoe	inflated, black, glassy		2
BD19	18	S3	2	43.44744	113.53388	N	margin	spiney pahoehoe	inflated, black, glassy		2
BD19	18	S3	3	43.44744	113.53388	N	margin	spiney pahoehoe	inflated, black, glassy		2
BD19	19	S1	1	43.44747	113.53403	Y	margin	spiney pahoehoe	blue, black, rusty red		2
BD19	19	S1	2	43.44747	113.53403	Y	margin	spiney pahoehoe	blue, black, rusty red		2
BD19	19	S1	3	43.44747	113.53403	Y	margin	spiney pahoehoe	blue, black, rusty red		2

BD19	19	S2	1	43.44747	113.53403	N	margin	spiney pahoehoe	blue, black, rusty red	2	LIBS shakey
BD19	19	S2	2	43.44747	113.53403	N	margin	spiney pahoehoe	blue, black, rusty red	2	LIBS shakey
BD19	19	S2	3	43.44747	113.53403	N	margin	spiney pahoehoe	blue, black, rusty red	2	LIBS shakey
BD19	19	S3	1	43.44747	113.53403	N	margin	spiney pahoehoe	blue, black, rusty red	2	
BD19	19	S3	2	43.44747	113.53403	N	margin	spiney pahoehoe	blue, black, rusty red	2	
BD19	19	S3	3	43.44747	113.53403	N	margin	spiney pahoehoe	blue, black, rusty red	2	
BD19	20	S1	1	43.44753	113.53351	N	margin	pahoehoe	breakout, sky blue, dark blue, wrinkles	<1	
BD19	20	S1	2	43.44753	113.53351	N	margin	pahoehoe	breakout, sky blue, dark blue, wrinkles	<1	
BD19	20	S1	3	43.44753	113.53351	N	margin	pahoehoe	breakout, sky blue, dark blue, wrinkles	<1	
BD19	20	S2	1	43.44753	113.53351	N	margin	pahoehoe	breakout, sky blue, dark blue, wrinkles	<1	
BD19	20	S2	2	43.44753	113.53351	N	margin	pahoehoe	breakout, sky blue, dark blue, wrinkles	<1	
BD19	20	S2	3	43.44753	113.53351	N	margin	pahoehoe	breakout, sky blue, dark blue, wrinkles	<1	

Sample ID	Sample #		GPS_N	GPS_W	Collected	Category	Morphology	Keywords	Surface Roughness (mm)	Notes
BD19	20	S3	1	43.44753	113.53351	Y	margin	pahoehoe	breakout, sky blue, dark blue, wrinkles	<1	
BD19	20	S3	2	43.44753	113.53351	Y	margin	pahoehoe	breakout, sky blue, dark blue, wrinkles	<1	
BD19	20	S3	3	43.44753	113.53351	Y	margin	pahoehoe	breakout, sky blue, dark blue, wrinkles	<1	

Table 2: Digitized notebook of field observations, sample numbers, and instrument data numbers of the Ross Flow at Lava Beds National Monument

Sample ID	Sample #	GPS_N	GPS_W	Collected	Category	Morphology	Keywords	Surface Roughness (mm)	Notes
T1	1	41.7747	121.54543	N	margin	pahoehoe	red, orange, weathered	5	eastern margin
T1	1	41.7747	121.54543	N	margin	pahoehoe	red, orange, weathered	5	eastern margin
T1	1	41.7747	121.54543	N	margin	pahoehoe	red, orange, weathered	5	eastern margin
T1	2	41.77471	121.54558	N	surface	pahoehoe	inflated, dark grey, weathered	3	
T1	2	41.77471	121.54558	N	surface	pahoehoe	inflated, dark grey, weathered	3	
T1	2	41.77471	121.54558	N	surface	pahoehoe	inflated, dark grey, weathered	3	
T1	3	41.7748	121.54593	N	surface	pahoehoe	orange, red,	2	

T1	3	41.7748	121.54593	N	surface	pahoehoe	orange, red,	2	
T1	3	41.7748	121.54593	N	surface	pahoehoe	orange, red,	2	
T1	4	41.7748	121.54601	N	surface	pahoehoe	orange, brown	2	
T1	4	41.7748	121.54601	N	surface	pahoehoe	orange, brown	2	
T1	4	41.7748	121.54601	N	surface	pahoehoe	orange, brown	2	
T1	5	41.77485	121.54602	N	margin	pahoehoe	red, brown, grey, weathered		western margin
T1	5	41.77485	121.54602	N	margin	pahoehoe	red, brown, grey, weathered		western margin
T1	5	41.77485	121.54602	N	margin	pahoehoe	red, brown, grey, weathered		western margin
T2	1	41.77553	121.54591	N	margin	pahoehoe	dark grey,	3	western margin
T2	1	41.77553	121.54591	N	margin	pahoehoe	dark grey,	3	western margin
T2	1	41.77553	121.54591	N	margin	pahoehoe	dark grey,	3	western margin
T2	2	41.77549	121.54569	N	surface	pahoehoe	breakout, red, brown, orange	four	
T2	2	41.77549	121.54569	N	surface	pahoehoe	breakout, red, brown, orange	four	
T2	2	41.77549	121.54569	N	surface	pahoehoe	breakout, red, brown, orange	four	
T2	3	41.77544	121.54546	N	surface	pahoehoe	squeeze up, orange, brown, weathered		
T2	3	41.77544	121.54546	N	surface	pahoehoe	squeeze up, orange, brown, weathered		
T2	3	41.77544	121.54546	N	surface	pahoehoe	squeeze up, orange, brown, weathered		
T2	4	41.7754	121.54537	N	vent	spatter	glassy, bomb, drooped, shiny, black, orange	one	west side of spatter cone

T2	4	41.7754	121.54537	N	vent	spatter	glassy, bomb, drooped, shiny, black, orange	one	west side of spatter cone
T2	4	41.7754	121.54537	N	vent	spatter	glassy, bomb, drooped, shiny, black, orange	one	west side of spatter cone
T2	5	41.77541	121.54533	N	vent	spatter	black, glassy, glazed,	3	
T2	5	41.77541	121.54533	N	vent	spatter	black, glassy, glazed,	3	
T2	5	41.77541	121.54533	N	vent	spatter	black, glassy, glazed,	3	
T2	6	41.77539	121.54531	N	vent	spatter	bomb, grey, gold,	2	east side of spatter cone
T2	6	41.77539	121.54531	N	vent	spatter	bomb, grey, gold,	2	east side of spatter cone
T2	6	41.77539	121.54531	N	vent	spatter	bomb, grey, gold,	2	east side of spatter cone
T2	7	41.77535	121.5452	N	surface	pahoehoe	inflated, dark grey, weathered	2	
T2	7	41.77535	121.5452	N	surface	pahoehoe	inflated, dark grey, weathered	2	
T2	7	41.77535	121.5452	N	surface	pahoehoe	inflated, dark grey, weathered	2	
T2	8	41.7752	121.54498	N	margin	pahoehoe	glassy, rope, shiny, translucent, grey, orange	2	eastern margin
T2	8	41.7752	121.54498	N	margin	pahoehoe	glassy, rope, shiny, translucent, grey, orange	2	eastern margin
T2	8	41.7752	121.54498	N	margin	pahoehoe	glassy, rope, shiny, translucent, grey, orange	2	eastern margin

T3	1	41.77551	121.54413	N	margin	spiney pahoehoe	weathered, orange, brown		5	eastern margin
T3	1	41.77551	121.54413	N	margin	spiney pahoehoe	weathered, orange, brown		5	eastern margin
T3	1	41.77551	121.54413	N	margin	spiney pahoehoe	weathered, orange, brown		5	eastern margin
T3	2	41.77567	121.54446	N	surface	pahoehoe	ropey, deflated, collapsed, orange, brown		5	
T3	2	41.77567	121.54446	N	surface	pahoehoe	ropey, deflated, collapsed, orange, brown		5	
T3	2	41.77567	121.54446	N	surface	pahoehoe	ropey, deflated, collapsed, orange, brown		5	
T3	3	41.77582	121.54491	N	surface	pahoehoe	breakout, orange, brown,			
T3	3	41.77582	121.54491	N	surface	pahoehoe	breakout, orange, brown,			
T3	3	41.77582	121.54491	N	surface	pahoehoe	breakout, orange, brown,			
T3	4	41.77593	121.54518	N	surface	pahoehoe	drained tube, grey, glassy,		2	
T3	4	41.77593	121.54518	N	surface	pahoehoe	drained tube, grey, glassy,		2	
T3	4	41.77593	121.54518	N	surface	pahoehoe	drained tube, grey, glassy,		2	
T3	5	41.77594	121.54561	N	margin	pahoehoe	ropey, orange, brown, grey, glassy		1	western margin
T3	5	41.77594	121.54561	N	margin	pahoehoe	ropey, orange, brown, grey, glassy		1	western margin

T3	5	41.77594	121.54561	N	margin	pahoehoe	ropey, orange, brown, grey, glassy	1	western margin
T4	1	41.7766	121.54588	N	margin	toothpaste pahoehoe	toe, orange, brown, grey,	2	western margin
T4	1	41.7766	121.54588	N	margin	toothpaste pahoehoe	toe, orange, brown, grey,	2	western margin
T4	1	41.7766	121.54588	N	margin	toothpaste pahoehoe	toe, orange, brown, grey,	2	western margin
T4	2	41.7765	121.5454	N	surface	pahoehoe	glazed, breakout, dark grey,	4	
T4	2	41.7765	121.5454	N	surface	pahoehoe	glazed, breakout, dark grey,	4	
T4	2	41.7765	121.5454	N	surface	pahoehoe	glazed, breakout, dark grey,	4	
T4	3	41.77638	121.5451	N	surface	pahoehoe	inflated, lava pond, glassy, black, orange, brown	4	
T4	3	41.77638	121.5451	N	surface	pahoehoe	inflated, lava pond, glassy, black, orange, brown	4	
T4	3	41.77638	121.5451	N	surface	pahoehoe	inflated, lava pond, glassy, black, orange, brown	4	
T4	4	41.77635	121.54503	N	vent	spatter	droopy, bomb, silver, glaze,	2	western side of cone
T4	4	41.77635	121.54503	N	vent	spatter	droopy, bomb, silver, glaze,	2	western side of cone
T4	4	41.77635	121.54503	N	vent	spatter	droopy, bomb, silver, glaze,	2	western side of cone

T4	5	41.77637	121.54492	N	vent	spatter	glassy, glazed, black,		3	secondary spatter rampart; broken XRF window
T4	5	41.77637	121.54492	N	vent	spatter	glassy, glazed, black,		3	secondary spatter rampart; broken XRF window
T4	5	41.77637	121.54492	N	vent	spatter	glassy, glazed, black,		3	secondary spatter rampart; broken XRF window
T4	6	41.77635	121.54476	N	vent	spatter	bomb, shiny, brown, glazed,		3	on top of spatter hook; broken XRF window
T4	6	41.77635	121.54476	N	vent	spatter	bomb, shiny, brown, glazed,		3	on top of spatter hook; broken XRF window
T4	6	41.77635	121.54476	N	vent	spatter	bomb, shiny, brown, glazed,		3	on top of spatter hook; broken XRF window
T4	7	41.77636	121.54473	N	vent	spatter	irredescent glaze, gold, red, pink,		3	broken XRF window; eastern side of cone
T4	7	41.77636	121.54473	N	vent	spatter	irredescent glaze, gold, red, pink,		3	broken XRF window; eastern side of cone
T4	7	41.77636	121.54473	N	vent	spatter	irredescent glaze, gold, red, pink,		3	broken XRF window; eastern side of cone
T4	8	41.77599	121.54438	N	surface	ropey pahoehoe	collapsed pond, matte black, orange, brown		6	broken XRF window
T4	8	41.77599	121.54438	N	surface	ropey pahoehoe	collapsed pond, matte black, orange, brown		6	broken XRF window
T4	8	41.77599	121.54438	N	surface	ropey pahoehoe	collapsed pond, matte black, orange, brown		6	broken XRF window

T4	9	41.7757	121.54414	N	margin	pahoehoe	breakout, cauliflower, dark grey, orange, brown	4	eastern margin
T4	9	41.7757	121.54414	N	margin	pahoehoe	breakout, cauliflower, dark grey, orange, brown	4	eastern margin
T4	9	41.7757	121.54414	N	margin	pahoehoe	breakout, cauliflower, dark grey, orange, brown	4	eastern margin
T5	1	41.77627	121.54358	N	margin	pahoehoe	orange, brown, weathered,	4	eastern margin
T5	1	41.77627	121.54358	N	margin	pahoehoe	orange, brown, weathered,	4	eastern margin
T5	1	41.77627	121.54358	N	margin	pahoehoe	orange, brown, weathered,	4	eastern margin
T5	2	41.77662	121.544	N	surface	ropey pahoehoe	cauliflower, glassy, black, matte, glazed, opalized	8	
T5	2	41.77662	121.544	N	surface	ropey pahoehoe	cauliflower, glassy, black, matte, glazed, opalized	8	
T5	2	41.77662	121.544	N	surface	ropey pahoehoe	cauliflower, glassy, black, matte, glazed, opalized	8	
T5	3	41.77686	121.54442	N	surface	slabby pahoehoe	pond, inflated, grey, orange, brown	3	
T5	3	41.77686	121.54442	N	surface	slabby pahoehoe	pond, inflated, grey, orange, brown	3	
T5	3	41.77686	121.54442	N	surface	slabby pahoehoe	pond, inflated, grey, orange, brown	3	

T5	4	41.77687	121.5445	N	vent	spatter	bomb, cow patty, glassy, grey	2	
T5	4	41.77687	121.5445	N	vent	spatter	bomb, cow patty, glassy, grey	2	
T5	4	41.77687	121.5445	N	vent	spatter	bomb, cow patty, glassy, grey	2	
T5	5	41.77702	121.54481	N	surface	slabby pahoehoe	grey, matte, orange, brown,	6	
T5	5	41.77702	121.54481	N	surface	slabby pahoehoe	grey, matte, orange, brown,	6	
T5	5	41.77702	121.54481	N	surface	slabby pahoehoe	grey, matte, orange, brown,	6	
T5	6	41.77711	121.54555	N	margin	slabby pahoehoe	breakout, dark grey, glassy, orange, brown,	4	western margin
T5	6	41.77711	121.54555	N	margin	slabby pahoehoe	breakout, dark grey, glassy, orange, brown,	4	western margin
T5	6	41.77711	121.54555	N	margin	slabby pahoehoe	breakout, dark grey, glassy, orange, brown,	4	western margin
T6	1	41.77782	121.54491	N	margin	slabby pahoehoe	black, glassy	8	western margin
T6	1	41.77782	121.54491	N	margin	slabby pahoehoe	black, glassy	8	western margin
T6	1	41.77782	121.54491	N	margin	slabby pahoehoe	black, glassy	8	western margin
T6	2	41.77777	121.54478	N	surface	pahoehoe	breakout, black, glassy,	10	
T6	2	41.77777	121.54478	N	surface	pahoehoe	breakout, black, glassy,	10	
T6	2	41.77777	121.54478	N	surface	pahoehoe	breakout, black, glassy,	10	

T6	3	41.77752	121.54424	N	surface	pahoehoe	breakout, grey, green, glassy,		5	
T6	3	41.77752	121.54424	N	surface	pahoehoe	breakout, grey, green, glassy,		5	
T6	3	41.77752	121.54424	N	surface	pahoehoe	breakout, grey, green, glassy,		5	
T6	4	41.77745	121.54391	N	vent	spatter	coated, draped, irredescent grey,		3	might not actually be spatter
T6	4	41.77745	121.54391	N	vent	spatter	coated, draped, irredescent grey,		3	might not actually be spatter
T6	4	41.77745	121.54391	N	vent	spatter	coated, draped, irredescent grey,		3	might not actually be spatter
T6	5	41.77734	121.54366	N	surface	pahoehoe	inflated, pond, shiny black, opalized		4	
T6	5	41.77734	121.54366	N	surface	pahoehoe	inflated, pond, shiny black, opalized		4	
T6	5	41.77734	121.54366	N	surface	pahoehoe	inflated, pond, shiny black, opalized		4	
T6	6	41.7771	121.5425	N	margin	ropey pahoehoe	breakout, dark black, wrinkled		3	eastern margin
T6	6	41.7771	121.5425	N	margin	ropey pahoehoe	breakout, dark black, wrinkled		3	eastern margin
T6	6	41.7771	121.5425	N	margin	ropey pahoehoe	breakout, dark black, wrinkled		3	eastern margin
T7	1	41.77774	121.54231	N	margin	ropey pahoehoe	matte black		5	eastern margin
T7	1	41.77774	121.54231	N	margin	ropey pahoehoe	matte black		5	eastern margin
T7	1	41.77774	121.54231	N	margin	ropey pahoehoe	matte black		5	eastern margin

T7	2	41.77785	121.54286	N	surface	pahoehoe	matte black, glassy, opalized	4	
T7	2	41.77785	121.54286	N	surface	pahoehoe	matte black, glassy, opalized	4	
T7	2	41.77785	121.54286	N	surface	pahoehoe	matte black, glassy, opalized	4	
T7	3	41.77806	121.54343	N	vent	spatter	golden, glassy, glazed, weathered,		not awesome data; might throw away
T7	3	41.77806	121.54343	N	vent	spatter	golden, glassy, glazed, weathered,		not awesome data; might throw away
T7	3	41.77806	121.54343	N	vent	spatter	golden, glassy, glazed, weathered,		not awesome data; might throw away
T7	4	41.77809	121.54347	N	vent	spatter	bomb, draped, glassy, black,	3	
T7	4	41.77809	121.54347	N	vent	spatter	bomb, draped, glassy, black,	3	
T7	4	41.77809	121.54347	N	vent	spatter	bomb, draped, glassy, black,	3	LIBS moved
T7	5	41.77808	121.54359	N	vent	spatter	bomb, irredescent, grey, shiny,	2	
T7	5	41.77808	121.54359	N	vent	spatter	bomb, irredescent, grey, shiny,	2	
T7	5	41.77808	121.54359	N	vent	spatter	bomb, irredescent, grey, shiny,	2	
T7	5	41.77808	121.54359	N	vent	spatter	bomb, irredescent, grey, shiny,	2	
T7	6	41.77814	121.54361	N	vent	spatter	glassy, black	7	
T7	6	41.77814	121.54361	N	vent	spatter	glassy, black	7	
T7	6	41.77814	121.54361	N	vent	spatter	glassy, black	7	

T7	7	41.7782	121.54397	N	surface	pillar	pond, collapsed, dark grey, stringy	10	
T7	7	41.7782	121.54397	N	surface	pillar	pond, collapsed, dark grey, stringy	10	
T7	7	41.7782	121.54397	N	surface	pillar	pond, collapsed, dark grey, stringy	10	
T7	8	41.77821	121.54403	N	surface	pahoehoe	degraded, grey, brown,	8	where we collected the "eclogite" sample; terrible surface; trash sample
T7	8	41.77821	121.54403	N	surface	pahoehoe	degraded, grey, brown,	8	where we collected the "eclogite" sample; terrible surface; trash sample
T7	8	41.77821	121.54403	N	surface	pahoehoe	degraded, grey, brown,	8	where we collected the "eclogite" sample; terrible surface; trash sample
T7	9	41.77836	121.54438	N	surface	spiney pahoehoe	collapsed pond, matte black, orange	4	
T7	9	41.77836	121.54438	N	surface	spiney pahoehoe	collapsed pond, matte black, orange	4	
T7	9	41.77836	121.54438	N	surface	spiney pahoehoe	collapsed pond, matte black, orange	4	
T7	10	41.77839	121.54449	N	surface	ropey pahoehoe	collapsed pond, breakout, dary grey, shiny,	3	
T7	10	41.77839	121.54449	N	surface	ropey pahoehoe	collapsed pond, breakout, dary grey, shiny,	3	

T7	10	41.77839	121.54449	N	surface	ropey pahoehoe	collapsed pond, breakout, dary grey, shiny,		3	
T7	11	41.77852	121.54481	N	margin	slabby pahoehoe	black,		2	western margin
T7	11	41.77852	121.54481	N	margin	slabby pahoehoe	black,		2	western margin
T7	11	41.77852	121.54481	N	margin	slabby pahoehoe	black,		2	western margin

Table 3: BD and RF pixel percentages for calculating % crystallinity using GIMP or ImageJ image processing

Sample name	Processer	Method	photo number	plag	olivine	glass	vesicles	oxides	apatite (BD)	high-Si glass	unknown	total
BD19-20-S3	Kari	Gimp	1	20.58	1.86	74.78	0.00	1.20	0.31			98.7
BD19-20-S3	Kari	Gimp	2	11.15	1.05	80.45	0.00	1.31	0.35	5.69		100.0
BD19-20-S3	Kari	Gimp	3	10.18	3.71	82.68	0.31	2.28	0.84	0.00		100.0
BD19-20-S3	Kari	Gimp	4	11.45	0.92	67.07	6.85	2.47	0.23	11.00		100.0
BD19-20-S3	Kari	Gimp	5	8.50	4.57	45.49	0.00	1.42	0.34	39.66		99.9
BD19-20-S3	Kari	Gimp	6	16.44	3.47	49.06	4.74	0.77	0.23	25.29		100.0
BD19-20-S3	Kari	Gimp	7	14.92	3.06	40.11	1.14	2.16	0.57	38.03		99.9
BD19-20-S3	Kari	Gimp	8	16.84	0.23	55.13	0.00	1.18	0.30	26.31		99.9
RF19-T2-5	Kari	Gimp	5	0.89	0.91	94.48	3.71	0.00				100.0
RF19-T2-5	Kari	Gimp	6	3.24	0.00	95.90	0.86	0.00				100.0
RF19-T2-5	Kari	Gimp	7	13.57	0.00	83.10	3.33	0.00				100.0
RF19-T2-5	Kari	Gimp	8	21.74	3.94	70.53	3.79	0.00				100.0
RF19-T2-5	Kari	Gimp	9	6.46	6.81	85.11	1.58	0.04				100.0
RF19-T2-5	Kari	Gimp	11	3.72	0.00	93.29	3.00	0.00				100.0

RF19-T2-5	Kari	Gimp	12	22.08	9.31	59.87	8.75	0.00				100.0
RF19-T2-5	Kari	Gimp	14	3.95	7.25	83.56	5.24	0.00				100.0
RF19-T2-5	Kari	Gimp	15	0.66	0.00	99.27	0.00	0.07				100.0
RF19-T2-4	Kari	GIMP	1	16.57	0.21	82.57	0.64					100.0
RF19-T2-4	Kari	GIMP	2	17.87	10.66	71.46	0.00					99.9
RF19-T2-4	Kari	GIMP	3	8.89	1.57	88.63	0.91					100.0
RF19-T2-4	Kari	GIMP	4	11.53	0.22	88.15	0.10					100.0
RF19-T2-4	Kari	GIMP	5	34.07	0.39	65.54	0.00					100.0
RF19-T2-4	Kari	GIMP	6	6.41	2.72	90.19	0.67					100.0
RF19-T2-4	Kari	GIMP	7	8.70	1.65	87.73	1.92					100.0
RF19-T2-4	Kari	GIMP	8	19.94	0.80	79.25	0.00					100.0
RF19-T2-4	Kari	GIMP	9	24.01	0.41	75.58	0.00					100.0
BD19-7-s1	Erika	ImageJ	1	43.10	20.10	26.65	3.34	6.81	0.00	0.00	0.00	100.0
BD19-7-s1	Erika	ImageJ	2 200x	29.33	23.36	23.73	11.49	12.09	0.00	0.00	0.00	100.0
BD19-7-s1	Erika	ImageJ	4 300x	58.50	12.82	24.57	0.00	4.11	0.00	0.00	0.00	100.0
BD19-7-s1	Erika	ImageJ	5 300x	45.91	17.21	28.09	0.00	8.79	0.00	0.00	0.00	100.0
BD19-7-s1	Erika	ImageJ	7 300x	57.72	14.58	20.59	0.00	7.11	0.00	0.00	0.00	100.0
BD19-7-s1	Erika	ImageJ	8 300x	31.95	19.26	37.83	0.53	10.43	0.00	0.00	0.00	100.0
BD19-7-s1	Erika	ImageJ	9 300X	50.23	10.82	26.89	0.00	5.88	6.18	0.00	0.00	100.0
BD19-7-s1	Erika	ImageJ	10 300X	52.82	11.58	22.57	0.00	6.30	6.73	0.00	0.00	100.0
BD19-7-s1	Erika	ImageJ	11 300X	60.72	8.63	17.87	0.00	4.87	7.90	0.00	0.00	100.0
BD19-19-S1	Kari	ImageJ	1	19.35	3.12	75.36	0.00	1.30	0.86			100.0
BD19-19-S1	Kari	ImageJ	2	16.71	3.78	76.35	0.25	1.98	0.94			100.0
BD19-19-S1	Kari	ImageJ	3	12.89	2.25	81.64	0.00	2.62	0.60			100.0
BD19-19-S1	Kari	ImageJ	4	19.46	6.52	70.60	0.00	2.87	0.55			100.0
BD19-19-S1	Kari	ImageJ	5	20.70	2.37	43.96	29.65	1.54	0.35	1.43		100.0
BD19-19-S1	Kari	ImageJ	6	16.37	5.02	68.60	4.78	4.05	1.18			100.0
BD19-19-S1	Kari	ImageJ	7	12.14	5.47	78.93	0.00	2.02	1.44			100.0

BD19-19-S1	Kari	ImageJ	8	11.48	4.56	82.38	0.00	1.00	0.59			100.0
BD19-15-S3	Kari	Image J	1	19.14	0.95	79.26	0.00	0.37	0.28			100.0
BD19-15-S3	Kari	Image J	2	13.79	2.70	82.44	0.00	0.84	0.23			100.0
BD19-15-S3	Kari	Image J	3	10.63	1.62	86.53	0.00	0.82	0.40			100.0
BD19-15-S3	Kari	Image J	4	14.66	3.29	80.44	0.00	0.60	1.00			100.0
BD19-15-S3	Kari	Image J	5	10.96	1.94	86.19	0.00	0.67	0.24			100.0
BD19-15-S3	Kari	Image J	6	19.33	1.04	78.27	0.00	1.06	0.30			100.0
BD19-15-S3	Kari	Image J	7	14.57	2.57	81.40	0.00	1.15	0.32			100.0
BD19-15-S3	Kari	Image J	8	17.38	2.06	79.59	0.00	0.79	0.17			100.0
BD19-12-S2	Kari	Image J	1	6.09	1.48	69.06	22.61	0.67	0.09			100.0
BD19-12-S2	Kari	Image J	2	5.73	1.59	75.19	16.05	0.99	0.45			100.0
BD19-12-S2	Kari	Image J	3	3.82	0.58	94.64	0.00	0.82	0.13			100.0
BD19-12-S2	Kari	Image J	4	6.94	1.24	91.26	0.00	0.40	0.16			100.0
BD19-12-S2	Kari	Image J	5	4.58	0.66	93.31	0.00	1.08	0.37			100.0
BD19-12-S2	Kari	Image J	6	6.39	0.00	92.39	0.00	1.09	0.13			100.0
BD19-12-S2	Kari	Image J	7	8.67	0.66	88.95	0.00	1.46	0.26			100.0
BD19-12-S2	Kari	Image J	8	11.64	2.63	85.37	0.00	0.30	0.06			100.0
BD19-10-S2	Kari	GIMP	1	16.18	2.03	79.78	0.05	0.55	0.46	0.93		99.9
BD19-10-S2	Kari	GIMP	2	6.38	1.69	89.59	0.00	1.75	0.59	0.00		99.9
BD19-10-S2	Kari	GIMP	3	9.29	3.07	85.85	0.00	1.56	0.22	0.00		99.9
BD19-10-S2	Kari	GIMP	4	9.84	0.99	86.65	0.00	0.76	0.29	0.00		98.5
BD19-10-S2	Kari	GIMP	5	7.36	1.61	89.28	0.00	1.22	0.52	0.00		100.0
BD19-10-S2	Kari	GIMP	6	11.63	4.55	81.64	0.00	1.82	0.35	0.00		100.0
BD19-10-S2	Kari	GIMP	7	6.52	1.00	90.01	0.00	1.42	1.06	0.00		100.0
BD19-10-S2	Kari	GIMP	8	7.90	1.79	82.42	0.69	2.36	0.06	4.77		100.0
BD19-11-S2	Kari	Image J	2	24.54	1.94	71.17	0.00	1.80	0.55			100.0
BD19-11-S2	Kari	Image J	3	14.23	2.28	79.99	0.00	2.97	0.52			100.0
BD19-11-S2	Kari	Image J	4	11.25	5.20	80.98	0.00	2.08	0.49			100.0

BD19-11-S2	Kari	Image J	5	11.57	5.68	79.73	0.00	2.34	0.67			100.0
BD19-11-S2	Kari	Image J	6	19.70	2.84	75.44	0.00	1.67	0.34			100.0
BD19-11-S2	Kari	Image J	7	15.01	2.99	79.77	0.00	1.65	0.58			100.0
BD19-11-S2	Kari	Image J	8	16.13	1.59	80.90	0.00	1.01	0.36			100.0
BD19-11-S2	Kari	Image J	9	18.66	3.78	75.61	0.00	1.43	0.52			100.0
RF19-T2-8	Kari	GIMP	2	3.14	0.00	92.69	4.17					100.0
RF19-T2-8	Kari	GIMP	14	4.91	0.00	84.05	11.04					100.0
RF19-T2-8	Kari	GIMP	15	1.35	0.00	93.09	5.55					99.9
RF19-T2-8	Kari	GIMP	16	28.87	0.00	61.00	10.12					100.0
RF19-T2-8	Kari	GIMP	17	8.96	0.00	89.96	1.08					99.9
RF19-T2-8	Kari	GIMP	18	30.38	0.00	66.45	3.17					99.9
RF19-T2-8	Kari	GIMP	19	0.40	29.98	64.62	4.99					99.9
RF19-T2-8	Kari	GIMP	20	12.96	4.39	77.69	4.95					99.9
RF19-T4-8	Kari	GIMP	1	0.25	0.00	99.75	0.00					100.0
RF19-T4-8	Kari	GIMP	2	2.69	0.00	97.31	0.00					100.0
RF19-T4-8	Kari	GIMP	3	7.10	0.42	92.48	0.00					100.0
RF19-T4-8	Kari	GIMP	4	11.22	0.00	88.78	0.00					100.0
RF19-T4-8	Kari	GIMP	5	68.61	0.13	30.13	1.12					100.0
RF19-T4-8	Kari	GIMP	7	18.84	6.47	74.68	0.00					99.9
RF19-T4-8	Kari	GIMP	8	13.87	0.31	85.64	0.00					99.8
RF19-T4-8	Kari	GIMP	9	44.10	10.64	45.25	0.00					99.9
RF19-T4-8	Kari	GIMP	10	2.61	0.00	97.39	0.00					100.0
RF19-T4-2	Kari	GIMP	2	17.87	10.66	71.46	0.00					99.9
RF19-T4-2	Kari	GIMP	6	8.89	1.57	88.63	0.91					100.0
RF19-T4-2	Kari	GIMP	7	11.53	0.22	88.15	0.10					100.0
RF19-T4-2	Kari	GIMP	8	34.07	0.39	65.54	0.00					100.0
RF19-T4-2	Kari	GIMP	9	6.41	2.72	90.19	0.67					100.0
RF19-T4-2	Kari	GIMP	16	8.70	1.65	87.73	1.92					100.0

| RF19-T4-2 | Kari | GIMP | 17 | 19.94 | 0.80 | 79.25 | 0.00 | | | | | 100.0 |
| RF19-T4-2 | Kari | GIMP | 18 | 24.01 | 0.41 | 75.58 | 0.00 | | | | | 100.0 |